NORTHWESTERN UNIVERSITY

Toward Rotational Cooling of Trapped SiO$^+$ by Optical Pumping

A DISSERTATION

SUBMITTED TO THE GRADUATE SCHOOL

IN PARTIAL FULFILLMENT OF THE REQUIREMENTS

for the degree

DOCTOR OF PHILOSOPHY

Field of Physics and Astronomy

By

David Tabor

EVANSTON, ILLINOIS

April 2014

ABSTRACT

Toward Rotational Cooling of Trapped SiO$^+$ by Optical Pumping

David Tabor

This thesis presents a scheme for preparation of trapped molecular ions with a high degree of internal state purity by optical pumping with a broadband pulse-shaped femtosecond laser; the internal structure of SiO$^+$ permits fast stepwise pumping through the tens of rotational levels populated in a room-temperature distribution. Two analyses, which guided the experimental implementation, are presented: (1) a novel method of quantifying anharmonicity in the trapping potentials, which limits the number of ions that can be trapped, and (2) a rate-equation simulation of the quantum state evolution during pumping. Experimental implementation of pulse shaping and its characterization are discussed, as is the molecular spectroscopy used to reference this light to the rotational cooling transitions. Internal state analysis can be performed using resonance enhanced multiphoton dissociation.

Table of Contents

List of Tables

List of Figures

CHAPTER 1

Laser Cooling and Trapping

In this experiment, $^{138}Ba^+$ is cooled and trapped as a diagnostic tool for the apparatus as well as to permit SiO^+ loading to be visually confirmed. The first two sections of this chapter summarize some basics of Ba^+ structure and the formalism of radiofrequency (rf) Paul traps. Much greater detail on these topics is available in the literature and not repeated here. The final section of this chapter summarizes the sources of heating experienced by a trapped ion in some detail; it is foundational to the discussion in Ch. 2.

1.1. Laser Cooling of Ba^+
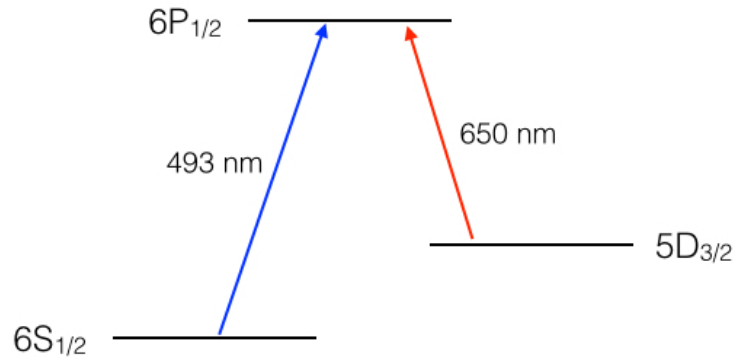
Figure 1.1. Ba^+ level diagram indicating transitions used in laser cooling.

The levels of $^{138}Ba^+$ involved in laser cooling are diagramed in Fig. 1.1. From the ground $6S_{1/2}$ state, 493 nm light drives excitations to the $6P_{1/2}$ state. This excited state may decay back to the $6S_{1/2}$ state, or alternatively it can decay to the $5D_{3/2}$ state. The

relative branching ratio between these two channels is $\Gamma_1/\Gamma_2 \approx 12$ MHz / 4 MHz ≈ 3. (A decay to $5D_{5/2}$ is also possible, but the rate is negligible in comparison to the other two channels. Other than these three, no other channels are present.) The line widths reported here are measured by [26].

The 493 nm $6S_{1/2} \rightarrow 6P_{1/2}$ transition is referred to as the cooling transition and in this experiment is provided by a frequency-doubled Ti:sapphire laser (Toptica DLPro 123). Repumping along the $5D_{3/2} \rightarrow 6P_{1/2}$ transition at 650 nm is produced by an *extended cavity diode laser* (ECDL) (Toptica DLPro 123).

Repumping of the Zeeman substructure of these transitions requires both σ^+ and σ^- polarizations to be present in the 650 nm repumping beam. Experimentally, a Helmholtz coil is used to define a quantization axis, and linearly polarized 650 nm light is oriented at $45°$ to this axis. The decomposition of this orientation along the quantization axis contains both σ^+ and σ^- components.

1.2. The RF Paul Trap

Ion trapping by radiofrequency (rf) electric fields was first demonstrated in 1954 by Paul in a trap with hyperbolic electrodes [29]. Attempts to maximize the field-free trapping volume led to the development of the linear Paul trap by Prestage in 1989 [31]. Although less harmonic than hyperbolic traps, the field-free central axis of linear traps often make theirs the preferred geometry for experiments involving multiple laser-cooled ions, including precision spectroscopy [34, 21], quantum information processing [13, 19], and cavity quantum electrodynamics applications [14].

A linear quadrupole ion trap (Fig. 1.2) is formed from four parallel cylindrical electrodes of radius r_e, held at a separation r_0, with an rf voltage signal applied to the electrodes. The resulting electric field confines the ion motion radially; axial confinement (in the $\hat{z}$-direction) is provided by endcap electrodes (not shown in Fig. 1.2), to which a static voltage is applied.

Near the trap center, the electric potential is given by

$$\phi(x, y, z, t) \quad = \quad \frac{V_{rf} cos(\Omega_{rf} t)}{r_0^2}(x^2 - y^2) +$$

(1.1)
$$\frac{\kappa V_{ec}}{z_0^2}(\frac{2z^2 - x^2 - y^2}{2})$$

where V_{rf} and Ω_{rf} are the voltage and frequency of the applied rf drive, V_{ec} is the static voltage applied to the endcap electrodes, z_0 is half the distance between the endcap electrodes, and κ is a geometric factor. While this description is accurate near the trap center and along the z-axis, significant deviations can occur elsewhere in the trap interior.

The radial motion of an ion in the potential of Eq. (1.1) is described by the Mathieu differential equations, and the stability of this motion is expressed using Mathieu parameters which depend only on V_{rf}, V_{ec}, Ω_{rf}, κ, and the charge-to-mass ratio q/m. Solutions to the Mathieu equations contain regions of parameter space where ion motion is stable [27], and trap parameters are chosen to operate in one such stable region.

The motion of a trapped ion can be described approximately as a superposition of micromotion, in which the ion oscillates at the rf frequency, with secular motion, in which the ion oscillates in a time-independent pseudopotential $\tilde{\phi}_{rf}(x, y, z)$ at slower secular frequencies ω_x, ω_y, and ω_z. An analytic relationship exists between the time-dependent
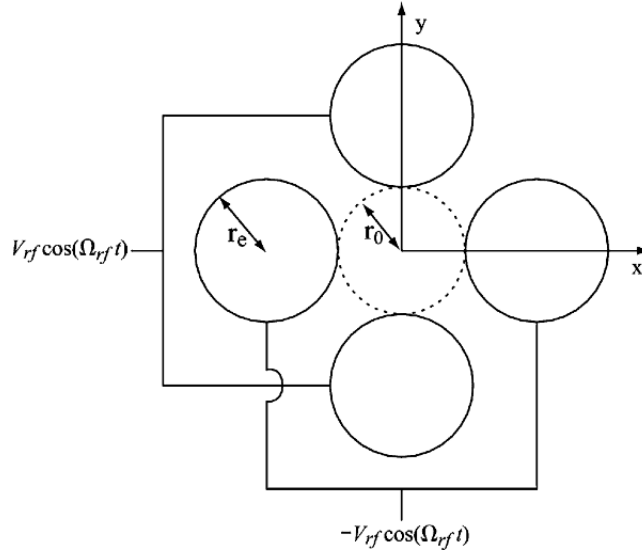
Figure 1.2. End view of a linear quadrupole trap. A sinusoidally varying voltage is applied to the rod electrodes, with one pair held 180° out of phase with the other.

rf potential and the time-independent pseudopotential [**7**]:

$$(1.2) \qquad \tilde{\phi}_{rf}(x, y, z) = \frac{q}{4m\Omega_{rf}^2} |\nabla \phi_{rf}(x, y, z, t = 0)|^2$$

The endcap electrodes generate a potential ϕ_{ec}, and the total potential governing secular motion is

$$(1.3) \qquad \phi_{trap} = \tilde{\phi}_{rf} + \phi_{ec}.$$

1.3. Heating of Trapped Ions

When the thermal energy of a trapped ion cloud is cooled sufficiently below the repulsive Coulomb interaction energy, the ions settle into a Coulomb crystal with geometry defined by the trapping potential [**49, 20**]. Crystallization of certain atomic ion species with

closed-cycle electronic transitions can be accomplished directly by laser cooling [9, 32]; crystallization of other species (e.g., molecular ions) can be accomplished sympathetically by laser cooling of a co-trapped atomic species [3] or *in situ* formation from a pre-cooled reactant [28]. Crystallization can be prevented by various heating mechanisms.

Although radial and axial micromotion vanish, respectively, along the trap axis and at $z = 0$, a large crystal necessarily extends beyond these regions. Micromotion heating results from the transfer of micromotion energy into secular energy, which leads to an elevated secular temperature. Although the scaling is non-trivial, simulations show that the micromotion heating rate strongly increases with micromotion amplitude and with secular temperature [37, 36]. As a crystal grows, additional ions are held at locations with increasingly strong rf fields, causing them to experience increasingly large micromotion. The resulting heating limits the minimum obtainable temperature for a crystal of a given size, and eventually prevents further crystal growth.

Nonlinear resonance heating can occur if a resonance condition is satisfied between secular frequencies and the rf drive frequency. For linear Paul traps, the condition is

$$(1.4) \qquad n_x\omega_x + n_y\omega_y + n_z\omega_z = \Omega_{rf}$$

where n_x, n_y, and n_z are integers [8]. The corresponding condition for a single particle in a hyperbolic trap has been derived [44], with the resonances weakening with larger n. This behavior has been confirmed in both hyperbolic traps [2] and linear traps [8]. For sufficiently cold trapped samples, it is understood that the frequency of the center of mass (COM) modes, or other normal modes, should be used in Eq. (1.4) rather than the single-particle frequencies [50]. For an infinitely long linear Paul trap, or for a small

crystal in a finite trap, where the axial rf drive vanishes, a non-deforming crystal is only expected to be heated on resonances with $n_z = 0$. However, a crystal which is large enough to sample axial fringing fields near the endcaps is expected to be excited also by resonances with $n_z > 0$.

Anharmonicity in the trapping potential causes the mode frequencies to shift as a crystal grows and samples less harmonic regions of the trap potential. Eventually, the anharmonicity-shifted mode frequencies of a growing crystal will meet the resonance condition of Eq. (1.4), and some level of heating will occur, potentially halting further crystal growth.

Even for a crystal of definite size, it is non-trivial to predict the precise response when it is swept through a given nonlinear heating resonance. Predicting the heating response in the non-equilibrium scenario of a growing crystal, as anharmonic frequency shifts cause it to cross a resonance, is yet more complicated. Modeling of the heating rates and whether crossing a given subharmonic resonance will actually melt a crystal or prevent further growth is beyond the scope of this analysis.

CHAPTER 2

Comparison of Trap Geometries

A trap capable of growing large Coulomb crystals is desirable for many types of experiment; in particular, for precision spectroscopy, large crystals improve the rate at which statistics are collected, often directly improving the achieved precision. This chapter describes an original method [42] for quantifying the susceptibility of a trap geometry to the two heating effects (micromotion heating and nonlinear resonance heating) described in Ch. 2. The axial component of micromotion, which leads to first-order Doppler shifts along the preferred spectroscopy axis in precision experiments, is also compared.

2.1. Geometries to be compared

Four different linear trap implementations are compared (Fig. 2.1, with corresponding voltage given in Table 2.1): a conventional in-line endcap design with two different voltage configurations (designs A and B), a plate endcap design (design C, similar to a design analyzed in Ref. [30]), and an original rotated endcap design (design D). In all trap designs, $z_0 = 8.5$ mm, $r_0 = 4$ mm, and $r_e = 4.5$ mm, with r_0 and r_e chosen to agree with the optimal ratio $r_e = 1.14511r_0$ for minimizing the leading-order contribution to anharmonicity in the rf potential [33]. Design C uses thin circular plates of radius $2r_e + r_0$ as endcap electrodes, with a 2 mm radius hole left for axial optical access. Design D has four small cylindrical endcap electrodes of radius 1.75 mm, rotated 45° around the z-axis; the central axes of these endcap electrodes are on the same radius as the central axes
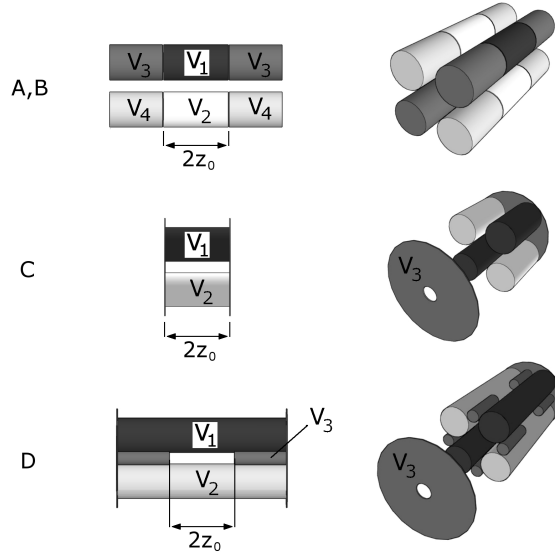
Figure 2.1. Trap designs analyzed in this chapter. Designs A and B share the same geometry, but differ in applied voltages. In the offset view at right, designs C and D are shown with the nearest plate endcap pulled away from the rest of the trap to allow the trap interior to be seen.

Table 2.1. Operating voltages applied in different trap designs. Here $V(t) = +V_{rf}cos(\Omega_{rf}t)$.

	V_1	V_2	V_3	V_4
A	$V(t)$	$-V(t)$	V_{ec}	V_{ec}
B	$V(t)$	$-V(t)$	$V_{ec} + V(t)$	$V_{ec} - V(t)$
C	$V(t)$	$-V(t)$	V_{ec}	N/A
D	$V(t)$	$-V(t)$	V_{ec}	N/A

of the rf electrodes. All numerical simulations presented here use values corresponding to ^{138}Ba$^+$ ($q = 1.602 \times 10^{-19}$ C, $m = 2.292 \times 10^{-25}$ kg) and our operating rf frequency ($\Omega_{rf} = 2\pi \times 3.00$ MHz).

The potential resulting from grounding all electrodes except the endcaps is denoted ϕ_{ec} and ϕ_{rf} is likewise defined for the rf electrodes. Both are found using the finite element

method to solve the Laplace equation, with the trap geometries discretized by the meshing software Gmsh [12].

To allow evaluation of the potentials at locations not on the mesh, the numerical solutions are fitted to an expansion in associated Legendre polynomials

$$\phi_{fit}(r, \theta, \phi) = \sum_{l=0}^{l_{max}} \sum_{m=-l_{max}}^{l_{max}} C_{lm} \; r^l \; P_l^m(cos \; \theta)$$

(2.1)
$$\times \begin{cases} cos(m\phi) & \text{for } m \geq 0 \\ \\ sin(m\phi) & \text{for } m < 0. \end{cases}$$

Terms with odd values of l and m are excluded from our fitting due to symmetry.

An analytic form of the gradient of Eq. (2.1) is straightforward to find using

$$\frac{\partial P_l^m(cos \; \theta)}{\partial \theta} =$$

(2.2)
$$\frac{l \; cos \; \theta \; P_l^m(cos \; \theta) - (l+m)P_{-l}^m(cos \; \theta))}{\sqrt{1 - cos^2\theta}},$$

which can be derived from a more general identity given by [1]. Fitting the Laplace solutions to the above expansion thus permits efficient evaluation of ϕ_{fit} or its gradient $\nabla\phi_{fit}$ at arbitrary location from the coefficients $\{C_{lm}\}$. In this way, the pseudopotential $\tilde{\phi}_{rf}$ and ϕ_{ec} are determined up to the scaling set by choosing V_{rf} and V_{ec}. Choices of these voltages, shown in Table 2.2, are made to equalize the single particle secular frequencies ω_z and ω_r across all designs at experimentally reasonable values $\omega_x = \omega_y = 2\pi \times 418$ kHz and $\omega_z = 2\pi \times 18.9$ kHz.

Table 2.2. V_{rf} and V_{ec} used in comparisons and calculated value of κ for each trap.

Trap Design	V_{rf} (volts)	V_{ec} (volts)	κ
A	800	5.0	0.15
B	800	5.0	0.15
C	800	2.7	0.27
D	800	51	0.014

Single particle secular frequencies are calculated by evaluation of $\tilde{\phi}_{rf}$ and ϕ_{ec} along a radial or axial trace through the origin from $r=-\frac{r_0}{2}$ to $r=+\frac{r_0}{2}$ or $z=-\frac{z_0}{2}$ to $z=\frac{z_0}{2}$ respectively. The resulting values fit a polynomial whose quadratic coefficient rapidly converges with finer discretization of the domain or increase of the polynomial fitting order. The values of $\kappa = \sqrt{2qC_2/m}$ are also found from this quadratic coefficient C_2 (see Tbl. 2.2).

The effect of inaccuracy in the Laplace solutions is estimated by observing convergence of calculated values such as κ with increasing meshing density, which is found to cause variation in all reported results of less than a few percent unless otherwise noted as we approach the highest mesh densities eventually used – of order 10^6 nodes for all designs. Tuning of other parameters, such as the fitting order l_{max} in Eq. (2.1), is found to cause negligible variance by comparison.

2.2. Micromotion amplitude

As described in Ch. 2, micromotion-induced heating can limit crystal growth, though the dynamics are complex. In this section, trap designs are compared by the amplitude of micromotion, computed for a single particle as a function of position, without attempt to specify where the growth of this quantity limits crystal size. The $\hat{z}$-components, which can limit the resolution of precision spectroscopy, are also compared.
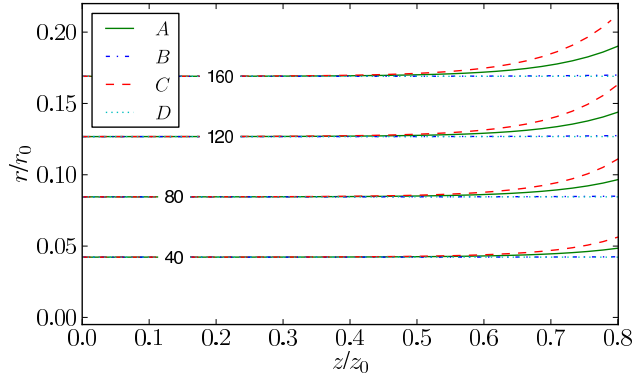
Figure 2.2.   Contour plots of total micromotion amplitude, labeled in microns. Designs B and D are indistinguishable at this scale.

Micromotion amplitude is computed from ϕ_{rf} as follows. The electric field created by the rf electrodes may be written as

(2.3) $$\overrightarrow{\mathbf{E}}(x,y,z,t) = \overrightarrow{\mathbf{E}}_{\mathbf{0}}(x,y,z)cos(\Omega_{rf}t).$$

For an ion held in place in a stationary crystal, in the limit of small micromotion amplitude $\overrightarrow{\mathbf{E}}_{\mathbf{0}}$ may be taken as constant as the ion moves, and the micromotion of the ion is harmonic with amplitude

(2.4) $$A(x,y,z) = \frac{q}{m\Omega_{rf}^2}|\nabla\phi_{rf}(x,y,z,t=0)|$$

With V_{rf} as set in Table 2.2, $\phi_{rf}(x,y,z,t=0)$ is used to calculate the resulting total micromotion amplitude $A(x,y,z)$. The resulting micromotion contour is plotted in Fig 2.2. All designs are comparable in the amplitude of total micromotion for any realistic trapping volume.

The $\hat{z}$-components of micromotion are also computed by considering only the $\hat{z}$-component of $\nabla\phi_{rf}$ in Eqn. 2.4. Due to the smallness of these values (several orders

Table 2.3. RMS average axial micromotion amplitudes over the cylindrical volume $r < 500$ μm, $|z| < z_0 = 8.5$ mm. Listed values for A and C change by no more than several percent when Laplace solutions are calculated over an order of magnitude in grid density. Values for B and D change by up to tens of percent. For averaging, the volume is discretized by a Cartesian grid with $h = 20$ μm, which is verified to be sufficiently dense.

Trap Design	RMS Axial Micromotion Amplitude (μm)
A	1.5
B	0.04
C	2.9
D	0.08

of magnitude smaller than the total amplitude) numerical convergence comparable to Fig. 2.2 is not observed. Rather than plot contours, we compute the root mean square (RMS) average over a large trapping volume for each design in Table 2.3, producing a single quantity whose convergence is verified.

No difference in micromotion heating rate is expected among the different designs, since total micromotion amplitudes are comparable. Indeed, in all cases axial micromotion amplitudes are much smaller than total amplitudes, indicating that rf-fringing should not limit crystal growth for these designs. The actual limit on crystal size due to micromotion heating is difficult to estimate, but it can in principle be found from molecular dynamics simulations.

Axial micromotion, quantified by RMS averaging over a volume bounding any realistic crystal, is at least than an order of magnitude smaller in designs B and D (in which the rf electrodes extend to $z > z_0$) than in A and C (in which the rf electrodes end at $z = z_0$). Since axial micromotion results from fringing of the rf fields, these differences are expected, given the different rf boundary conditions at $z = \pm z_0$. Given a conservative interpretation of the observed convergence of this average, B and D may be said to have

comparable axial micromotion, while the situation in A is much worse and in C worse still.

2.3. Nonlinear resonance susceptibility

As described in Ch. 1.3, anharmonicity in the trapping potential causes nonlinear resonances to eventually be triggered by a growing crystal. This section introduces a method for quantifying this effect, based on the shifts in value of the center of mass (COM) mode frequency as a growing crystal samples increasing amounts of anharmonicity. A previous analysis by the Marseille group (Pedregosa et. al. [30]) specified a single quantity describing the radial trap anharmonicity averaged over a trapped sample. The Marseille approach has the utility of providing a single figure of merit by which to compare different trap designs; however, it does not consider axial anharmonicity (potentially important for long crystals) or provide an estimate of what level of anharmonicity is acceptable in order to avoid heating resonances. The analysis presented here is similarly simple to calculate, and at the cost of not providing a single figure of merit, seeks to include axial anharmonicity and to provide a mechanism for determining whether a trap is sufficiently harmonic to safely work with crystals of some size.

For a zero-temperature crystal in a perfectly harmonic trapping potential, the COM oscillation frequency is the same as the secular frequency of a single particle. However, if the temperature of the crystal is nonzero or if the trapping potential is anharmonic, the crystal deforms during oscillation, and the COM frequency and single particle frequency are no longer equal. (Space charge shifts, which are well-understood in the limit of each ion moving independently in a background potential describing the distributed

charge of the other ions, occur at high temperatures but not for a non-deforming crystal.) Molecular dynamics (MD) simulations can find the COM frequency under finite temperature conditions, but this approach is computationally intensive for a large crystal. To understand the effects of anharmonicity with less computational overhead, this analysis approximates the crystal as non-deforming, which of a non-deforming crystal.

Since it is difficult to determine whether crossing a heating resonance will limit crystal growth or cause other deleterious effects, in the current analysis, we take a conservative approach of attempting to design a trap in which a growing crystal will avoid low-order resonances altogether. We consider the anharmonicity-induced shifts of the COM frequencies for a non-deforming crystal; the non-deforming approximation is exact in the zero-temperature limit. In light of the resonant condition of Eq. (1.4), considering the COM frequency shifts provides a simple estimate of when trap anharmonicity could limit crystal growth. Other modes of higher order than the COM mode can also be excited by nonlinear resonance heating, but the COM shifts are easily calculable and set the scale for anharmonicity-induced shifts in higher modes.

A single ion in a zero temperature crystal is held in place by the cancellation of two forces: that due to the trap potential F_{trap} and that due to the Coulomb repulsion of all other ions in the trap F_{ions}. In the approximation that the crystal does not deform during oscillation, F_{ions} remains constant while $F_{ions} + F_{trap}$ is, to leading order, a restoring force resulting in simple harmonic motion.

F_{trap} can be calculated from ϕ_{trap}, evaluated on a grid (x_i, y_j, z_k) where $x_i = ih, y_j = jh$, and $z_k = kh$; i, j, k are integers; $h = 50 \ \mu$m is the step size used in this calculation. The restoring force for small displacements in the $\hat{z}$ direction, at fixed x_i and y_j is then

calculated as follows. By geometrical symmetry ϕ_{trap} is an even function of z, so the numerically calculated values can be fitted to a polynomial series of even terms:

(2.5)
$$\phi_{trap}(z)\Big|_{x_i, y_j} = C_0 + C_2 z^2 + ... + C_{10} z^{10}$$

The axial force on an ion in a potential of this form is

(2.6)
$$F_{trap}(z) = -q(2C_2 z + ... + 10 C_{10} z^9).$$

For an ion whose equilibrium location in a crystal is $z = z_k$, an expansion of F_{trap} about z_k gives

(2.7)
$$F_{trap}(z) = F_{trap}(z_k) + (z - z_k) F'_{trap}(z_k) + ...$$

Since $z = z_k$ is an equilibrium position for this ion, the Coulomb force due to all other ions F_{ions} must exactly cancel the first term of this expansion. In the approximation of a non-deforming crystal, F_{ions} is a constant, and the total force on the ion is

(2.8)
$$F_{trap} + F_{ions} = -q \left(2C_2 + ... + 90 C_{10} z_k^8 \right) (z - z_k)$$

(2.9)
$$\equiv -k_z \Big|_{x_i, y_j, z_k} (z - z_k),$$

where $k_z|_{x_i, y_j, z_k}$ is a local spring constant describing the strength of the axial restoring force on an ion about its equilibrium location (x_i, y_j, z_k). As seen from Eqs. (2.6) and (2.8), when $z_k \neq 0$, anharmonic terms of the trap potential contribute to the spring constant k_{z_k}.

The restoring force on a crystal is the sum of the restoring forces on the individual ions. For a non-deforming crystal, the result is oscillatory motion at a frequency set by the averaged local spring constants, with the average taken over the ion locations. In our calculation we average instead over the grid locations, for points interior to the crystal volume. In this way, the axial COM frequency for a crystal is estimated from ϕ_{trap} and a specified crystal geometry. The COM frequencies for radial motion are computed by the same method using a fitting polynomial of the same order.

Fig. 2.3 shows the change in axial COM frequency in each trap design as crystal volume grows. Crystal extent is determined by evaluation of ϕ_{trap} on a Cartesian grid with spacing $h = 50$ μm, with all points below a fixed cutoff included, and ion number is then determined by the ion density [10],

$$(2.10) \qquad \rho = \frac{m\epsilon_0}{q^2}(\omega_z^2 + 2\omega_r^2),$$

where ω_z and $\omega_r = \omega_x = \omega_y$ are the single particle secular frequencies. This density is assumed constant; the anharmonicity-induced position dependence is negligible.

Radial COM shifts are also computed, with fittings made to radial rather than axial traces of ϕ_{trap}. Over the volume occupied by the largest crystals in Fig. 2.3, no difference among the designs can be determined at our level of computational accuracy. Varying all calculation parameters bounds radial COM shifts at no more than tenths of a percent.

The size of COM frequency shifts during crystal growth, found here to differ among the considered designs, is an indicator for the effect of nonlinear resonance heating on trap operation. As the experimenter grows a crystal, adding ions continuously from an ion source, small COM frequency shifts (say a few percent) are not expected to present
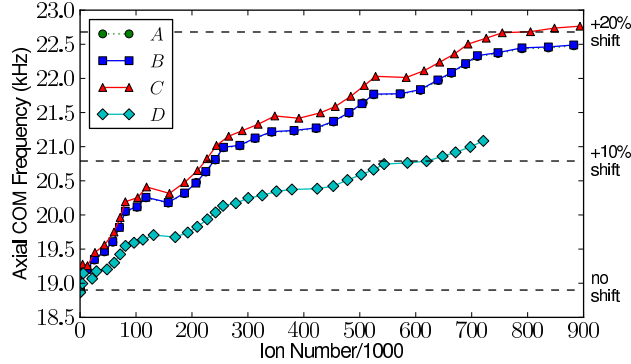
Figure 2.3. COM axial secular frequency as a function of ion number. Curves for Designs A and B are overlapping. Crystals are grown until their axial extent reaches $\pm z_0/2$; for equal length, design D grows an appreciably smaller crystal. Ripples result from finite evaluation grid size.

significant challenge. The COM frequencies are unlikely to shift onto a nonlinear resonance during the intermediate stages of crystal growth, and the experimenter can load the largest crystal possible before checking if different voltages increase the maximum crystal size. For larger size-dependent shifts, trapping voltages could, in principle, be dynamically tuned to avoid resonances as the crystal grows, but dynamic tuning would become increasingly challenging for larger shifts. Thus the designs A, B, and C, which exhibit large COM frequency shifts, are expected to be more less suitable for growing large crystals than design D.

As an example of these concerns, we note that for the frequencies considered in this study, excitation of the nonlinear resonance $|n_x| + |n_y| = 7$, $n_z = 3$ is expected when the axial COM frequency increases by 5-10%, a shift which occurs in design D only for a crystal containing tens of thousands more ions than in other designs. (Resonances of this order and higher have been observed experimentally in a linear trap [8].) The expected ability of D to load more ions than the other designs before exciting this resonance is a
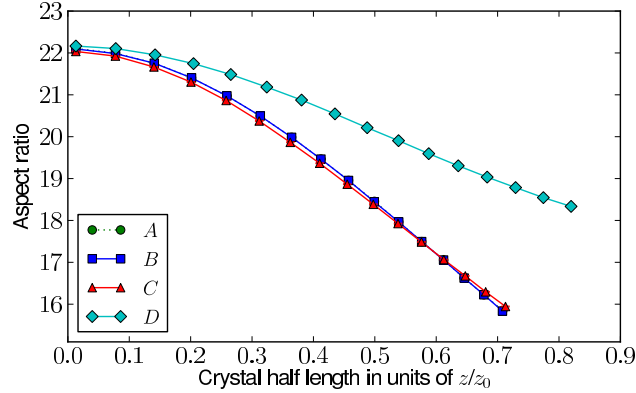
Figure 2.4. Aspect ratio as a function of crystal size, with aspect ratio estimated by comparison of the heights of the radial and axial potentials along $\hat{x}$ and $\hat{z}$ respectively. A is overlapped by B and not visible.

direct result of the smaller axial COM shifts in D. In general, since the rotated endcap design D has the smallest axial COM shifts it is expected to be the least susceptible to nonlinear resonance heating.

A consideration of aspect ratios during crystal growth can provide some physical understanding of the behavior of design D. For a perfectly harmonic trapping potential, the aspect ratio of a crystal will be independent of size and equal to the ratio of the secular frequencies, which in these traps were tuned to be equal in the harmonic trapping region. Accordingly, eventual differences in aspect ratio are due to different degrees of anharmonicity sampled by the trapped ions. In Fig. 2.4, the expected change in aspect ratio during crystal growth is plotted for each design, calculated by a simple comparison of the heights of the radial and axial potentials along $\hat{x}$ and $\hat{z}$ respectively. The tendency of design D to maintain larger aspect ratio than other designs explains the ion numbers seen in Fig. 2.3; at equal length, the crystals in designs A, B and C are radially wider than D and so contain more ions. Intuitively, the tendency of D toward radially narrower

crystals helps explain the smaller axial COM shifts in D, since the regions nearer the $\hat{z}$ axis are expected to be more harmonic than those radially further away.

The ripples in Fig. 2.3 caused by the finite size of the evaluation grid do not interfere with the conclusion that the COM frequency shift in D is smaller than in the other designs, as the trend is clear at much sparser grids, where the ripples are even more pronounced. The Laplace solutions are found to converge sufficiently to determine the COM shifts to within a few percent, and all other parameters–the associated Legendre and polynomial series fitting orders and the evaluation grid density–are adjusted until the resulting convergence in COM frequency shifts is not limiting.

CHAPTER 3

Pulse Shaping for Rotational Cooling

Pulse-shaping is the processes by which a spectrally broad light source is manipulated to remove certain frequency components. In the context of rotational cooling of SiO^+, this pulse can then be used to drive rotational cooling transitions while avoiding rotational heating transitions. The Orsay group has previously used pulse-shaping of a femtosecond laser to demonstrate vibrational cooling of neutral alkali dimers created from ultracold atoms [**43**][**40**]. Rotational cooling was not possible in that context because the spacing of rotational lines in these dimers is much smaller than the 1 cm^{-1} pulse-shaping resolution the Orsay group achieved. (Subsequent discussion makes use of the frequency unit *wavenumber* $\nu = 1/\lambda$ expressed in cm^{-1}. A frequency interval of 1 cm^{-1} = 30 GHz.)

3.1. Theory of Pulse Shaping

The optical scheme used for pulse-shaping is schematically depicted in Fig. 3.1 for a spectrally broad input and in Fig. 3.2 for a monochromatic input. The former of these input types produces the pulse-shaping relevant for rotational cooling; the latter is presented here only for explanatory purposes.

The optical configuration used is termed the *4–f Fourier-transform layout* [**46**][**39**]. In this configuration, the path of a optically broad input pulse may be understood as follows. The input, assumed to be collimated, is dispersed off a grating. The first order diffraction is collected by a cylindrical lens of focal length f, placed a distance f from

the grating so as to collimate the first order beam. At a distance f further beyond the lens ($2f$ from the grating), a physical mask is placed which has the effect of blocking some spectral components, while permitting others to pass. A mirror is placed directly behind the mask (adding no extra path length in the ideal case), and the pulse is reflected back through the $2f$ distance to the grating. The diffraction of this pulse off the grating produces the useable output.
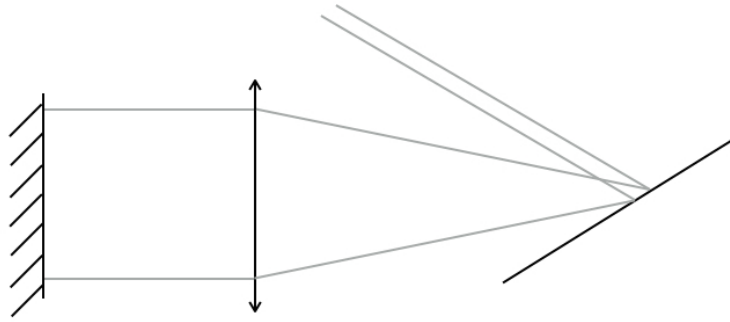
Figure 3.1. Schematic depiction of optics for pulse-shaping, with optical path traced for a spectrally broad input. This input produces the pulse-shaped output relevant for rotational cooling. The 4-f Fourier-transform layout is used.
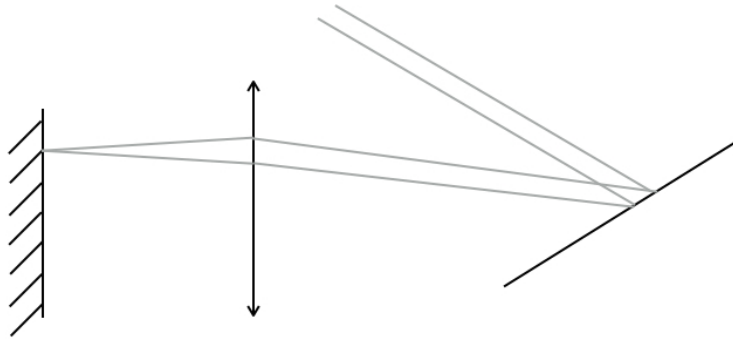
Figure 3.2. Schematic depiction of optics for pulse-shaping, with optical path traced for a monochromatic input. This situation is not experimentally implemented but is presented here as an aid to understanding the theoretical treatment of pulse-shaping. The 4-f Fourier-transform layout is used.

The action of pulse shaping can be better understood by reviewing the $4-f$ configuration while considering a monochromatic input; the experimentally-useable broad input is then understood as the superposition of many such monochromatic inputs. This case is depicted in Fig. 3.2. The monochromatic input, again assumed collimated, diffracts off the grating. The first-order diffraction remains collimated, unlike the spectrally broad case, and so after passing through the lens, it is focused and produces a beam waist of minimal size w_0 at a distance of f from the lens ($2f$ from the grating).

The spot size of a monochromatic beam at the Fourier plane is

$$(3.1) \qquad w_0 = \frac{\cos \theta_{in}}{\cos \theta_d} \frac{\lambda f}{\pi w_{in}}.$$

The incident angle of the input light to the grating is denoted θ_{in}, and the outgoing angle of the first-order diffraction is denoted θ_d, both measured relative to the normal from the grating surface. Many gratings are designed so that first-order diffraction is maximized when $\theta_{in} \approx \theta_d$, and the configuration is called *near-Littrow*.

The monochromatic spot size at the Fourier plane, w_0 may be compared to the spatial dispersion, α, which quantifies the spatial separation of different colors at the Fourier plane and has units of distance per unit frequency [25].

$$(3.2) \qquad \alpha = \frac{\lambda^2 f}{cd \cos \theta_d}$$

where d is the grating period. The diffraction-limited FWHM spectral resolution of pulse-shaping is then [25]

$$(3.3) \qquad \delta\nu_d = (\ln 2)^{1/2} \frac{w_0}{\alpha} = (\ln 2)^{1/2} \frac{\cos \theta_{in}}{\pi w_{in}} \frac{cd}{\lambda}.$$

The quantity $\delta\nu_d$ conceptually represents the "sharpness" of the pulse shaping cutoff, and, to allow rotational cooling, must be sufficiently narrow to selectively drive certain SiO^+ transitions while not driving others.

3.2. Application to Rotational Cooling

A diatomic molecule possesses three internal degrees of freedom: its electronic configuration, its vibrational motion (stretching and compressing of the internuclear bond) and its rotational motion (about an axis normal to the internuclear bond). The energy scales associated with these three degrees of freedom are very different, with electronic states having the largest energy separations of the three (on the scale of a visible photon, typically) while rotational spacings are the smallest (in SiO^+ of order 100 GHz). The scheme described here involves excitations from the ground electronic, ground vibrational state (in which all the room temperature thermal population resides and is distributed among the rotational levels) to an excited electronic state that also has v=0. This is termed a 0-0 transition for the vibrational states involved. The electronic states are described by a notation analogous to atomic term symbols of the form $^{2S+1}L_J$ but using the good quantum numbers of the diatomic molecule. The analogue to L is Λ, the component of electronic oribtial angular momentum along the internuclear axis. In molecular term symbols, Σ is used for $\Lambda = 0$, Π for $\Lambda = 1$, and Δ for $\Lambda = 2$, extending the atomic S, P, D... convention.

The ground electronic state of SiO^+ is $X^2\Sigma^+$. Standard diatomic nomenclature denotes the ground electronic state the "X-state" and excited electronic states are successively labeled A, B, C, etc. (The terminology originates from early emission spectroscopy of the "A-band", "B-band," and so on.)

The B state in SiO^+ is also $^2\Sigma^+$ and the driving excitations transitions used in the proposed rotational cooling scheme are $B \leftarrow X$. The B-X 0-0 band is comprised of p-branch ($\Delta J = -1$) transitions and r-branch ($\Delta J = +1$) transitions. Fig. 3.3 reviews

this structure and the resulting allowed relaxations in a simplified picture in which spin-rotation coupling is ignored. Pulse-shaping permits rotational cooling of SiO^+ by driving only the p-branch transitions, which remove rotational quanta. After relaxation, which may occur along either channel, the molecule can either have experienced $\Delta J = 0$ or $\Delta J = -2$. See Fig. 3.3.

The remainder of this section addresses several concerns omitted in the above simplified picture.

Vibrational leaks to $X(v > 0)$

Due to the highly diagonal Franck-Condon factors of the B-X 0-0 transition, population in $B(v'=0)$ is much much more likely to decay to $X(v''=0)$ than to excited vibrational

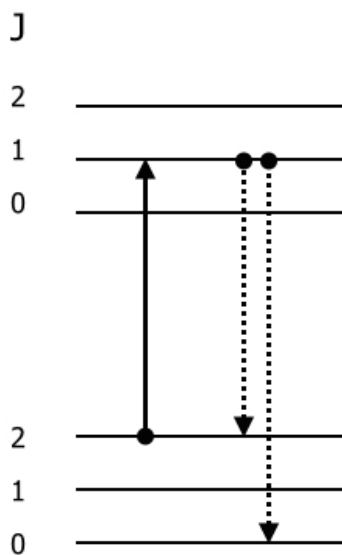Figure 3.3. Example of an absorption-emission cycle when a p-branch transition is driven. From its excited state, the molecular ion may decay either to its original state or to a state with less rotational energy than it originally had. Over many such cycles, a rotationally hot molecular ion can be stepwise cooled. The upper and lower rotational manifolds are the $B(v'=0)$ and $X(v''=0)$ states respectively.

states in X. (Standard nomenclature denotes the upper state quantum numbers with a single ′ and lower state quantum numbers ″.) This fact permits the stepwise rotational cooling described above, as several dozen absorption-excitation cycles are required to cool the rotationally hottest initial population.

A simple script adding up Einstein A factors for leaks to non-cycling states was used to confirm that vibrational leaks are sufficiently slow; leakage to any of X(v=1-7) is estimated to take typically >7000 absorption-excitation cycles. The rate-equation simulation of Ch. 7 can answer questions of this type, but the script (included in the Appendix) is useful for quick and approximate estimations of leak rates and branching ratios.

The Intervening A State

Decays from the B state to the A state remove population from the cooling scheme, and due to the large energy separation of the B and A states, one might guess this leak to be rapid. Differences in dipole moment functions cause the B→A decay to be slower than expected and, critically, slower than the A→X rate; no population build up in the A state is expected. The rate-equation simulation in Ch. 7 addresses this issue more throughly.

Spin-Rotation Coupling and The Parity Barrier

In $^2\Sigma$ states, spin-rotation coupling causes each J level to be split into two levels–one with J increased by 0.5 and the other with J decreased by 0.5 from its original value. The resulting ladder of rotational states, along with the resulting parities, is shown in Fig. 3.4.

The dipole-allowed E1 transitions used for rotational cooling follow the selection rule $\Delta P = \pm 1$. After both the absorption and spontaneous emission events have occurred, the molecule has thus returned to the same parity in which it started. For the room temperature distribution, the total population in states with positive parity is very close

to 50%, and likewise for negative parity states. Therefore, the rotational cooling scheme described here ideally produces a rotationally cooled population split between the ground states of each parity.

Although the positive parity ground state is the singlet $N = 0$, $J = 1/2$, there are actually two negative parity ground states in SiO^+, as the $N = 1$ state is a doublet, split by spin-rotation coupling into states with $J = 0.5$ and $J = 1.5$. Selection rules prevent pumping the higher of these two states into the lower by the scheme outlined here.

A planned extension to this experiment is to add a microwave source driving a purely rotational excitation within the $X(v = 0)$ manifold. This single photon process transfers population from one parity to the other. All population would then accumulate in the singlet positive parity ground state.

Pulse shaping resolution

Pulse-shaping is necessary to to drive only the p-branch but not the r-branch because the two branches are separated by 5 cm^{-1}. This level of pulse shaping resolution approaches the limits of what has been demonstrated, but was produced and characterized in for this experiment as described in the following section.
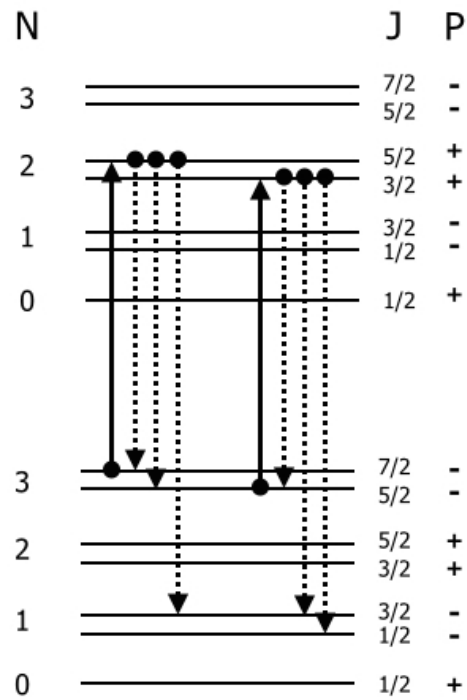
Figure 3.4. After experiencing an absorption-emission cycle, the parity of the quantum state is unchanged. Population that begins in a positive parity state is cooled to the N=0, J=1/2 state. Population that begins in a negative parity state is cooled to either of the $N = 1$, $J = 1/2$ state or the $N = 1$, $J = 3/2$ state.

3.3. Experimental Implementation

A SpectraPhysics MaiTai laser with an 80 MHz pulse repetition rate provides the input for pulse shaping. The output is tuned to a central wavelength 770 nm with several nm linewidth. The output is doubled by a BBO crystal placed at the focus of a 50 mm-50 mm telescope, with a maximum achieved doubling efficiency of 1.9 W/3.0 W = 64%. Tbl. 3.1 lists the part numbers and specifications for the experimentally realized setup.

A commercial spectrometer (Ocean Optics HR4000) was used to characterize the output of the experimental pulse-shaping setup. A comparison of the spectrum of the femtosecond laser before and after pulse-shaping, measured with the commercial spectrometer, is given in Fig. 3.5.

Figure 3.5. Spectrum of femtosecond laser before and after pulse shaping as measured by a commercial spectrometer with 10 cm^{-1} resolution.

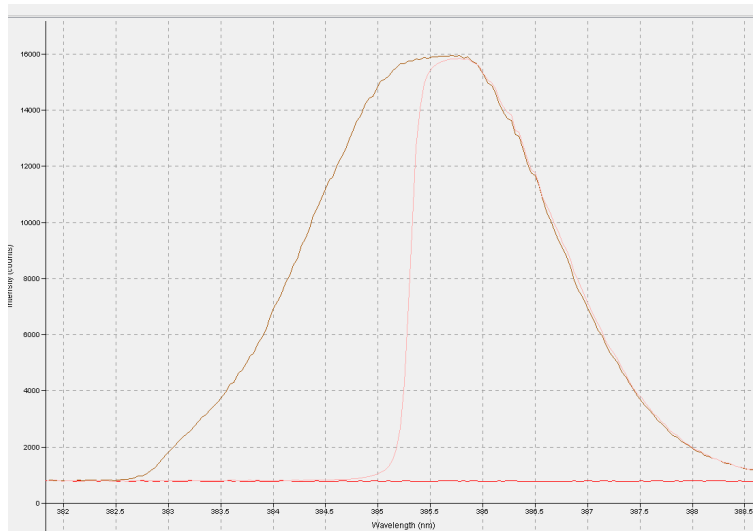The output from pulse shaping is extracting by a vertical offset from the input beam. Polarization control was not used to extract the output beam because the grating diffraction efficiency, which dominates optical power losses in pulse shaping, is polarization-dependent.

Grating Selection

The primary considerations in grating selection are groove density and first order diffraction efficiency. As seen in Eqn. 3.2, higher grove density improves shaping resolution, although this is only true up to a limit beyond which the fundamental grating condition

$$(3.4) \qquad\qquad d(sin\alpha + sin\beta) = m\lambda$$

cannot be satisified. (α and β are the incoming and outgoing incidence angles to the normal. Note that setting α to zero recovers the familiar form used for normal incidence.) Since the left-hand side cannot exceed $2d$, λ sets a limit on the largest d that will permit a valid solution with $m = 1$. The higher order $m \geq 2$ diffracted beams are not useful in this context due to their greatly lessened diffraction efficiency.

Implementation of Pulse Shaping

A schematic of the pulse shaping implemented for this experiment is given in Fig. 3.6. The direct fs laser output at 770 nm is frequency doubled to 385 nm (covering the B-X 0-0 band) by a BBO crystal (Type I non-critical phase matching) positioned at the focus of the telescope pair L1/L2.

A telescope pair L3/L4 follows this section. Adjustment of this telescope ratio is used to maximize the beamsize at L5, which improves shaping resolution. Expanding the beam
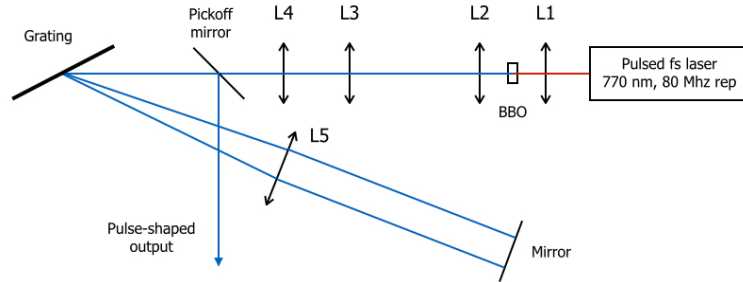
Figure 3.6. Schematic of pulse shaping setup.

to cover the lens L5 to its edges was found to cause abberation in the shaped frequency spectrum, however, and the implementation discussed here eventually used a beam that covered most but not all of the lens L5.

Both ruled and holographic gratings were tested, and the holographic grating was found to also induce aberration in the shaped spectrum that was sensitive to the difference in incoming and outgoing beam angles. Since we used vertical separation to extract the outgoing beam, a ruled grating, which was found not to have this issue, was preferred.

Implementation of Homebuilt Spectrometer

The resolution of the commericial spectrometer is 10 cm^{-1}, making it useful for initial pulse shaping alignment but insufficient to resolve a shaping cutoff as sharp as the one desired in this experiment. Accordingly, a homebuilt spectrometer with greater resolution was built.

The homebuilt spectrometer setup is similar to that for pulse shaping, except at the Fourier plane the mask and mirror are replaced by a CCD. At this location, the frequency distribution has been mapped onto spatial position, so a line CCD directly measures the spectrum of the pulsed shaped beam. The implementation in this experiment uses a line spectrometer with 8 μm pixel spacing (correspondence with a technician confirmed this

is the pixel center-to-center distance), which corresponds to a frequency resolution 8 μm / (40 μm per cm^{-1}) = 0.2 cm^{-1}, comfortably sufficient to measure a pulse shaping cutoff with ones of cm^{-1} width.

Optimization of homebuilt spectrometer is performed similarly to the pulse shaping setup. Optics are positioned coarsely, then adjusted to bring the measurement into good agreement with the pulse shaped spectrum measured by the commercial spectrometer.

Additional calibration and optimizaiton of the home built spectrometer was performed by sweeping the dye laser frequency and observing the resulting shift in peak location on the line CCD, as shown in Fig. 3.8. The dye laser output is expected to be effectively monochromatic at this frequency scale, since its linewidth is listed as 0.06 cm^{-1}, although a verification using far-field Airy ring patters (the linewidth measurement technique described in the manual) was not performed.
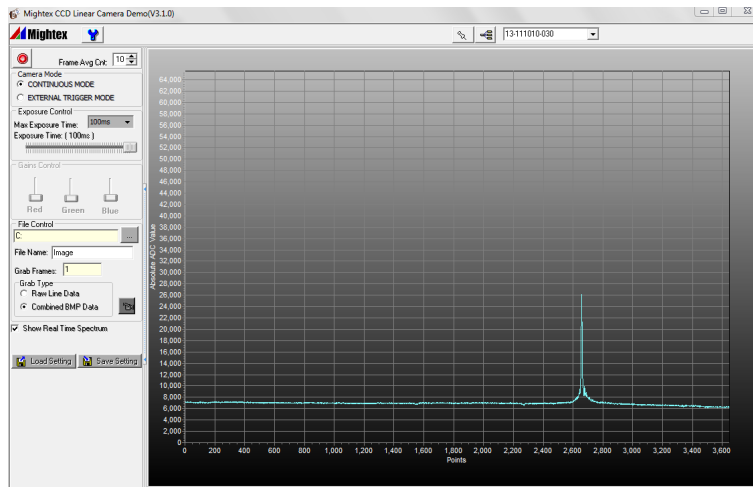
Figure 3.7. Dye laser as observed on the homebuilt spectrometer. The linewidth of the dye laser is expected to be much less than the resolution of the spectrometer.
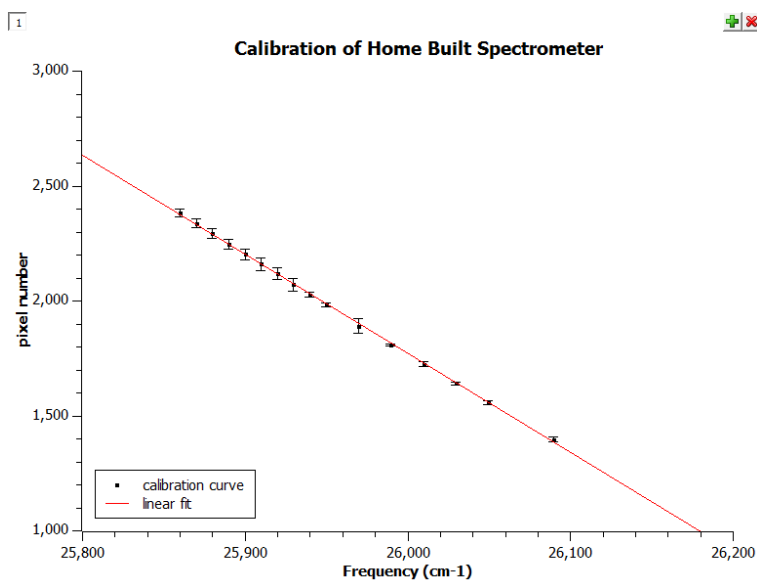
Figure 3.8. Calibration of the homebuilt spectrometer. A dye laser (expected to be monochromatic at this scale) is varied in frequency, and the resulting line CCD peak location is recorded.

Assuming the dye linewidth is as expected, the measurement in Fig. 3.7 shows a surprisingly large linewidth. Contact with a technician from the CCD supplier indicated that some bleedover between pixels is known to occur, resulting from scattering at the air-glass interface at the CCD surface. An additional bleedover effect also occurs in CCDs when a pixel is saturated, but this was avoided in the measurement discussed here.
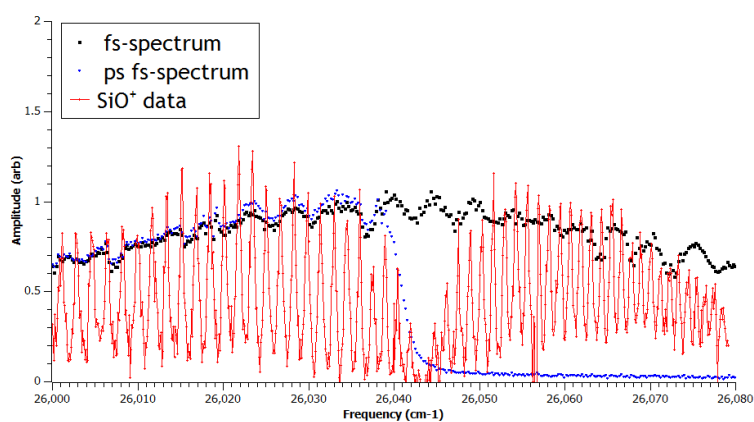
Figure 3.9. Homebuilt spectrometer measurement of pulse shaping output. Overlaid is the B-X 0-0 band measured using the spectroscpoy technique described in Ch. 8.

Name	Vendor	Model Number	Comment
Pulsed fs laser	Spectra Physics	MaiTai HP	Pulse shaping input
BK-7 spherical lens, f=50mm	Thorlabs	LA1131-B	L1. ARC covering 770 nm.
BBO crystal	Newlight	Custom	
UVFS spherical lens, f=50mm	Thorlabs	LA4148-UV	L2. ARC covering 385 nm.
UV Cylindrical lenses	Thorlabs	LJ4918-UV, e.g.	L3, L4.*
Posts, post holders, mounts	Thorlabs	Various	
1" UV square mirror	Thorlabs	PFSQ10-03-F01	Placed at Fourrier plane
Ruled Grating	Richardson	33009BK01-170R	3600 grooves per mm
Translation stage	Thorlabs	PT1	Longitudinal tuing of L5, mirror
Translation stage, precision	Thorlabs	PT1A	Transverse razor motion
Razor blade, mount			Mask in Fourier plane
Dye laser, 385 nm	Sirah	PSCAN-LG-1800	
Commercial spectrometer	Ocean Optics	HR4000	Useful for coarse alignment

Table 3.1. Parts list. Vendor part numbers confirmed accurate as of April 14, 2014. *Purchasing a variety of focal lengths from f=10 mm to f=100 mm, to allow later tuning of L3/L4 telescope ratio, is recommended.

CHAPTER 4

Rate Equation Simulation of Molecular Population Dynamics

4.1. Introduction and Motivation

Whereas laser cooling of atomic ions typically involves two or three quantum states, the vibrational and rotational degrees of freedom present in molecular ions cause many more states to be involved. The population dynamics relevant for rotational cooling therefore involves many more states than are easy to treat from a direct extension of the standard three-level "lambda" system. A rate-equation simulation, which treats states classically in that coherences are ignored, was developed to gain intuition regarding the cooling process.

The primary advantage of optical pumping for rotational cooling, as compared to the IR pumping methods which have been previously demonstrated [41] [38], is the rapid timescale—order μsec—on which cooling is achieved. To see that this μsec estimate is accurate under ideal circumstances, one can note that rotational cooling from $J'' = 40$ requires typically 40 excitation-relaxation cycles when only p-branch transitions are driven. (Decays to $X(v > 0)$ or to the A state are very slow comparatively.) The duration of this number of cycles is approximately $40 * 70$ nsec $= 3$ μsec. Understanding the factors contributing to this thermalization timescale, whose behavior might be unintuitive under non-ideal conditions, partly motivated the development of this simulation. $J'' = 40$ is

used as an estimate of the highest rotational level that needs to be cooled because $> 99\%$ of the thermal population is contained below this level, as can be seen as follows.

At room temperature, the internal states of SiO^+ equilibrate with the blackbody distribution with population contained entirely within the $X(v = 0)$ manifold. Approximating the molecule as a rigid rotor, Herzberg (III, 162) gives the rotational state distribution within a vibrational manifold as

$$(4.1) \qquad\qquad N_J \propto (2J + 1)e^{-B_e J(J+1)hc/kT}$$

with the distribution parameterized only by B_e, the rotational constant, and T, the blackbody temperature with which the population equilibrates [15]. As shown in Fig. 4.1, almost all the population is contained below $J = 40$, which is energetically below the $v = 1$ manifold, confirming that at $T = 300$ K the population is contained entirely within $X(v = 0)$.

An additional motivation for the simulation is the overlap of the p-branch of the 0-0 vibrational band, which must be driven for rotational cooling, with the 1-1 vibrational band. To a lesser degree, the 2-2 and higher $\Delta v = 0$ bands are overlapped as well. The effect of unwanted driving of bands other than 0-0 is tested by the rate-equation simulation.

The effect of suboptimal pulse shaping resolution can also be investigated. The separation of the B-X(0-0) p- and r-branches in SiO^+ is approximately $B_e = 4 \times 0.7$ cm^{-1} = 2.8 cm^{-1}, though achieving this resolution as well as confirming it by measurement are both separately difficult. A theoretical treatment of pulse shaping resolution and discussion of experimental characterization is given in Ch. 3. Setting the position of the pulse
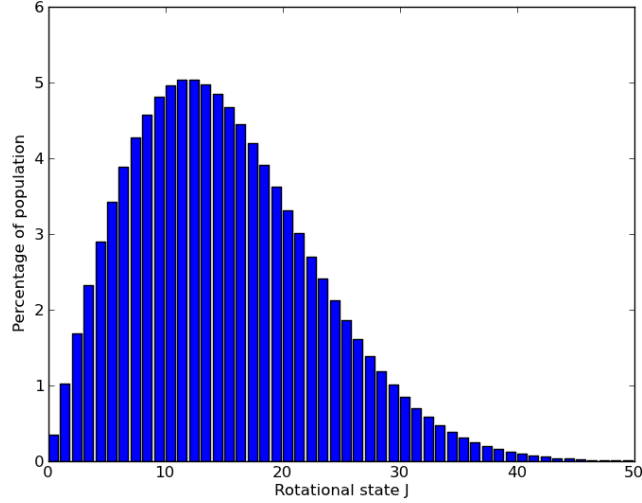
Figure 4.1. $T = 300$ K distribution of SiO$^+$ internal states. $B_e = 0.721$ cm^{-1}, as measured by Rosner [35], is used to generate this plot. $> 99\%$ of the population is contained below $J = 40$. Each J value corresponds to two quantum levels which differ by $\Delta K = 1$ except for $J = 0$ (see Ch. 4), though this detail has been ignored for simplicity in generating this figure.

shaping cutoff from reference spectroscopy is described in Ch. 6 and achievable precision is discussed. The rate-equation simulation can show the expected sensitivity of the cooling process to imprecision in cutoff positioning.

4.2. Methodology

As described quantitatively in Sec. 4.1, several dozen rotational levels of SiO$^+$ are populated at room temperature. Since each optical excitation causes at most $\Delta J = -1$, for rate-equation simulation to describe step-wise rotational cooling from the highest J levels involves a similar number of rotational levels in the $B(v = 0)$ manifold. Including in the simulation levels up to $J = 40$ in the $X(v = 0)$ manifold is sufficient to describe cooling from the room temperature distribution, as $> 99\%$ of the population is included in these levels (see Fig. 4.1). Since the cooling is step-wise, rotational levels up to $J = 40$ in $B(v = 0)$ are also required. In all simulations, vibrational levels from zero up to $v_{max} = 7$ are included for each of the three electronic states X, A, and B, resulting in a total of 1072 states. Each of these parameters which set the number of quantum levels included is verified to be sufficient by observing convergence to the values reported here as the number of quantum levels included is increased from below.

Einstein A coefficients are calculated using LEVEL 8.0 [22], with input energy separations from Ref. [5] and potential energy curves and dipole transition moment curves from Refs. [4, 48]. This work was done by Jason Nguyen. The resulting table of transitions includes up to $v'_{max} = v''_{max} = 7$ and $J'_{max} = J''_{max} = 5.5$. The current work extends this table of transitions up to $J'_{max} = J''_{max} = 40$ using scaling by Hönl-London factors. The original Nguyen table and the script used to generate this extended table are included as supplemental materials. The Hönl-London scaling process is described below.

Within a given vibrational band, the Einstein A coefficient of any rotational line may be calculated from the A coefficient for another rotational line by scaling by Hönl-London factors. This results from the fact that the matrix element which sets the A

coefficient is the same for these two transitions up to their Hönl-London factors—they have identical electronic and vibrational wavefunction overlaps. The script used to extend the original Nguyen table uses this concept to calculate the A coefficient for higher J levels by multiplying the known A coefficient of a lower J level by the appropriate ratio of Hönl-London factors.

The general formula for the Hönl-London factors is cumbersome, but simplifies for the particular case of $^2\Sigma^+-^2\Sigma^+$. The B-X transition in SiO$^+$ is of this type, and, from [45], the Hönl-London factors are

$$S_{N', \ J', \ N'', \ J''} = (2J' + 1)(2J'' + 1) \begin{pmatrix} N' & 1 & N'' \\ J'' & \frac{1}{2} & J' \end{pmatrix}^2 \times$$

(4.2)
$$(2N' + 1)(2N'' + 1) \begin{Bmatrix} N' & 1 & N'' \\ 0 & 0 & 0 \end{Bmatrix}^2$$

where parentheses denote the Wigner 3-j operation and curly brackets denote the Wigner 6-j operation.

The author is unaware of a standard numerical implementation for these Wigner operations, and since they involve factorials and recursively-calculated Clebsch-Gordon coefficients, computation for large values of angular momentum is nontrivial. The naïve implementation used in this calculation is included in the supplemental materials. It is confirmed to produce Hönl-London factors of the correct order of magnitude up to $J = 40$. (Due to summation and selection rules, the Hönl-London factor in this context is typically 1/3 and never exceeds one; it may be interpreted as a rotational branching ratio, and three decays are possible from any given excited state in a $^2\Sigma^+-^2\Sigma^+$ transition. See Ch. 4.) For

$J > 60$, however, numerical divergence is observed. A simulation at higher temperatures, such as the 1000's of K produced by ablation loading, would require attention to this issue.

The population evolution as a function of time is found by solving the set of coupled ordinary differential equations described by

$$\dot{\vec{x}} = D\vec{x} \tag{4.3}$$

where $\vec{x}$ is the vector of populations corresponding to each basis state.

The system of rate equations is generated from the list of allowed transitions as follows. First consider the simple case of a two level system in which a single transition is allowed. The full system of rate equations is

$$\frac{dx_2}{dt} = -A_{21}x_2 - B_{21}\rho(\omega_0)x_2 + B_{12}\rho(\omega_0)x_1$$

$$= B_{12}\rho(\omega_0) \cdot x_1 + [-A_{21} - B_{21}\rho(\omega_0)] \cdot x_2 \tag{4.4}$$

and

$$\frac{dx_1}{dt} = -B_{12}\rho(\omega_0) \cdot x_1 + [A_{21} + B_{21}\rho(\omega_0)] \cdot x_2. \tag{4.5}$$

By extension, for a full system of basis states $\vec{x}$,

$$\frac{dx_j}{dt} = \sum_i -A_{ki}x_k - B_{ki}\rho(\omega)x_i + B_{ik}\rho(\omega)x_k$$

$$+ \sum_k A_{jk}x_j + B_{jk}\rho(\omega)x_j - B_{kj}\rho(\omega)x_k \tag{4.6}$$

where the summation i is over the set of states for which a downward transition to j is allowed, and the summation k is over the set of states for which an upward transition to j is allowed. ρ quantifies the optical power available to drive the specified transition and is discussed in more detail below. The transition matrix elements D_{ji} are defined so that

$$(4.7) \qquad \frac{dx_j}{dt} = \sum_i D_{ji} x_i.$$

The resulting system of first-order ordinary differential equations in the form given by Eqn. 4.3 is solved by the numerical method `odeint`, called from the Python (v 2.7) package Scipy (v 0.12), which uses the `lsoda` method in the Fortran library `odepack`. Though the Scipy package is itself immature, it is merely a wrapper for well-established solving algorithmns.

From the table of transitions and their A coefficients, the B coefficients can be calculated directly.

$$(4.8) \qquad B_{21} = \frac{\pi^2 c^3}{\hbar \omega_{21}^3} \times A_{21}$$

$$(4.9) \qquad B_{12} = \frac{g_2}{g_1} B_{21}$$

A careful discussion of Eqn. 4.8 is given by [16]. Sources provide differing versions of the above formulae owing to different definitions of related quantities. The version used here is from [16], which also sets the definition of ρ to be optical energy density (energy

per volume) per unit frequency. The relation between ρ and optical intensity is then

$$(4.10) \qquad\qquad\qquad \rho(\omega) = cI(\omega)d\omega.$$

Here intensity I is optical power per unit area, also termed irradiance in some sources.

The driving radiation spectrum used in the simulation is that of an fs-laser whose output has been pulse shaped (see Ch. 3). The reference spectroscopy described in Ch. 6 was used to experimentally set the shaping parameters.

For the simulation, the arctan function is scaled so that the limiting values for large and small ω are zero and one respectively. The functional form used to model the pulsed shaped spectrum is that of a Gaussian multiplied by an *arctan* term that acts as a broadened step function (see Fig. 4.2). The sharpness of this effective step function is quantified by the width of the frequency interval in which the *arctan* term falls from 90% of its maximum value to 10% of this value.

$$(4.11) \qquad \rho(\omega) = \underbrace{Ae^{(\omega-\omega_0)^2/\sigma^2}}_{\text{unshaped laser spectrum}} \times \overbrace{\frac{1}{\pi}[\arctan(\alpha(\omega - \omega_{ps})) + \frac{\pi}{2}]}^{\text{effective step function}}.$$

Four cases are considered: two in which the pulse shaping cutoff is ideally positioned, but with varying shaping resolution, and two additional cases in which the pulse shaping cutoff is misplaced. In all cases, the intensity of the pulse is 250 mW/mm^2, corresponding to the measured optical power in our experimental setup focused into one mm^2. The FWHM of the pulse is set to 100 cm^{-1}, and the center of the unshaped gaussian is set to 26,000 cm^{-1}. The conditions are summarized in Tbl. 4.1.
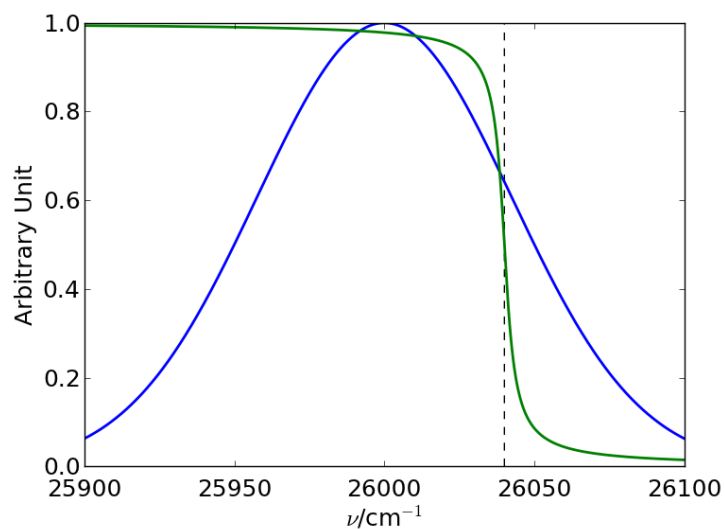
Figure 4.2. Gaussian and arctan function plotted separately. A vertical dotted line indicates the midpoint of the arctan cutoff.

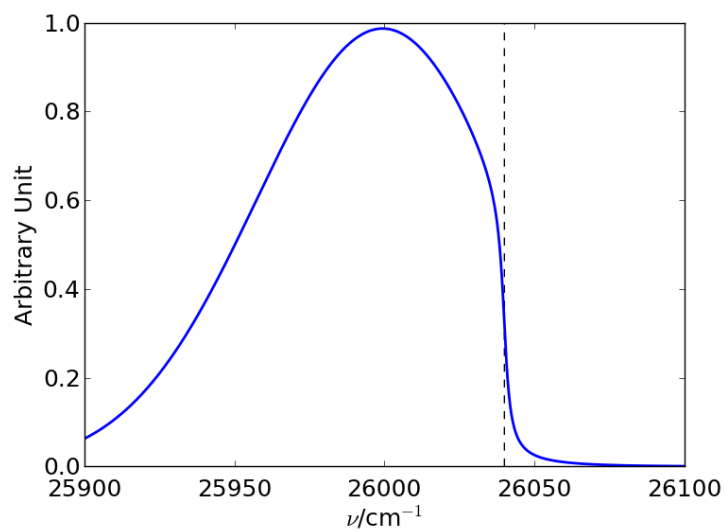Figure 4.3. Product of gaussian and arctan functions. A vertical dotted line indicates the midpoint of the arctan cutoff.

Table 4.1. Cases used in simulation.

Case	Description	ω_{ps} cutoff position / cm^{-1} (relative to band head)	90-10 cutoff width / cm^{-1}
(a)	Ideal	0	1
(b)	Broadened	0	10
(c)	Red-detuned	-10	1
(d)	Blue-detuned	+10	1

4.3. Results and Discussion

In case (a), the ideal case, the initial population is step-wise cooled into the ground states with a maximum of 89.9% of the population in the ground states after 140 μsec. After this time, population leaks from the ground states to vibrational excitations on a timescale of ms. This effect is caused by the width of the pulse shaping cutoff, which causes some r-branch transitions to be driven.

In case (b), in which the pulse shaping cutoff is broadened, more r-branch transitions are driven than in case (a), and the p-branch transitions nearest the band head are driven more slowly. The result is a smaller maximum ground state population (64.4% after 131 μsec) and a faster rate of sustained cycling due to driving the r-branch. Population accumulates in vibrationally excited states more rapidly than in (a) due to this increased cycling rate.

In case (c), several r-branch transitions are driven at full intensity, causing rapid depopulation of the ground states. The full p-branch is driven at full intensity however, so this population can again be cooled, and the resulting rate equilibrium causes a maximum ground state population of 17.9% after 111 μsec. The continued cycling of this population is stronger than in case (b), causing a comparatively more rapid buildup of population in vibrationally excited levels. Another symptom of the persistent cycling is the appreciable buildup of population in the B state.

In case (d), some p-branch transitions are driven only by the weak shoulder of the pulse shaping cutoff, and the r-branch is still further suppressed. Accordingly, slow step-wise cooling of the population occurs, with negligible accumulation in vibrationally excited states. Additionally, some non-negligible population accumulates in vibrationally excited

Figure 4.4. Simulation results for ideal pulse shaping. The maximum population collected in the three ground states is 89.9% after 140 μsec.

Figure 4.5. Simulation results for broadened pulse shaping. The maximum population collected in the three ground states is 64.6% after 131 μsec.

states during the first 100 μsec, but eventually is repumped; the 1-1 band overlaps the

0-0 band.

Figure 4.6. Simulation results for blue-detuned pulse shaping. The maximum population collected in the three ground states is 17.9% after 111 μsec.

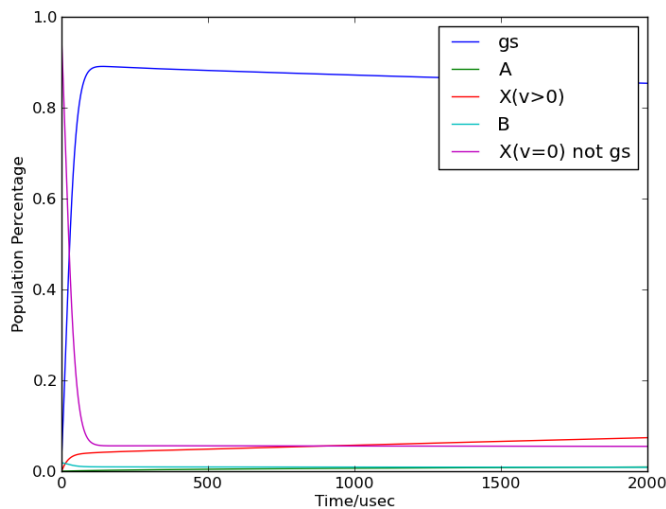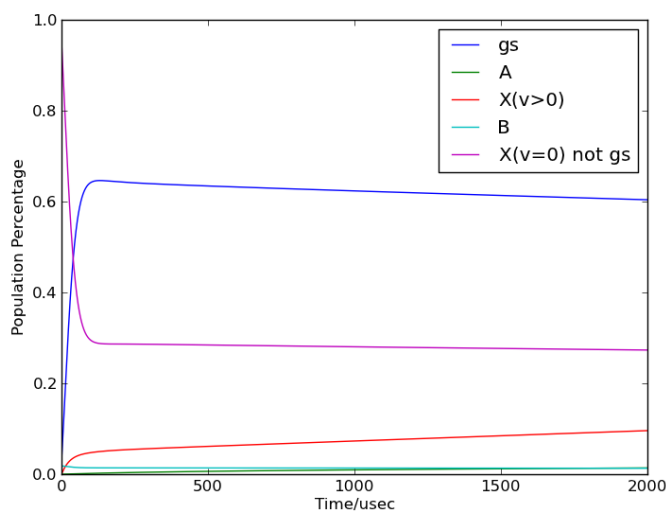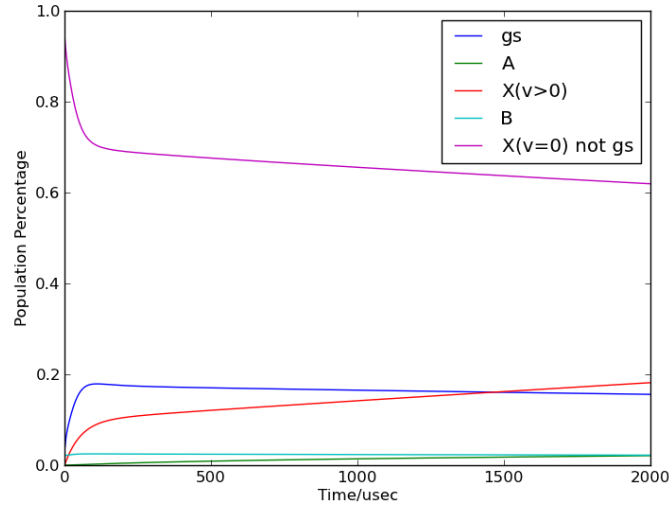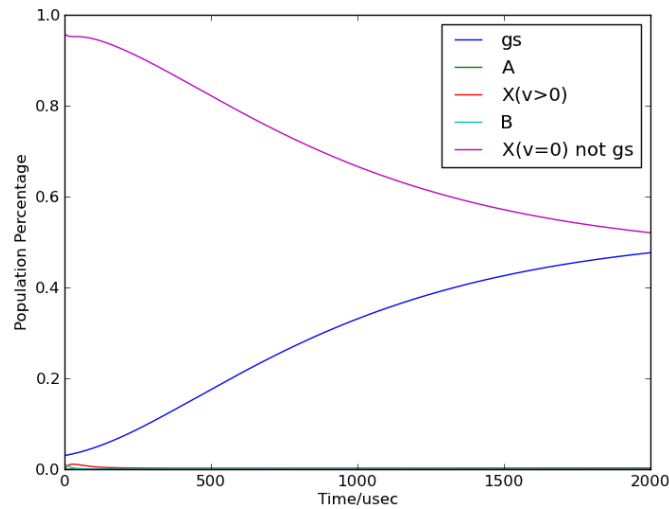Figure 4.7. Simulation results for red-detuned pulse shaping. The maximum population collected in the three ground states is 47.6% after 2000 μsec, which is the end of the simulation.

The simulation justifies the following conclusions. First, the effectiveness of rotational cooling is not strongly sensitive to pulse shaping resolution if the cutoff is properly positioned. In case (b), where the pulse shaping resolution is broadened to a 90-10 width of 10 cm^{-1}, nearly two thirds of the population collects in the ground states, an amount that should be detectable with only modest state readout effectiveness. The REMPD method of state readout is described in Ch. 5. Secondly, the effectiveness of rotational cooling is sensitive to the positioning of the pulse-shaping cutoff, affecting both the equilibrium population in the ground states as well as timescale on which this equilibrium is reached, as illustrated by cases (c) and (d). In these cases, the pulse shaping cutoff is misplaced by ± 10 cm^{-1}, which approximately the resolution with that a commercial spectrometer can be used to position the pulse shaping cutoff. A better method of transferring knowledge of the band head location from the reference spectroscopy to the pulse shaping setup must be used, or an experimental parameter space is created which much be searched. Finally, the overlap of the 0-0 band with higher order $\Delta v = 0$ bands is not problematic.

CHAPTER 5

Resonance Enhanced Multi-photon Dissociation

5.1. Overview

Rotational cooling of SiO^+ is verified by state-selective photodissociation, an established method called *resonance enhanced multi-photon dissociation* (REMPD). In its simplest version, this is a two-photon process, and in cases where the two photons are the same color, the process is called 1+1 REMPD. If they are different color, it is called $1+1'$ REMPD. In either case, the first photon drives an excitation from a target rovibrational state to another bound state. The second photon then drives population from this bound state to the continuum. The photoionization is state-selective because the first photon alone lacks the necessary energy to cause photodissociation; only the population originally in the target rovibrational state has the chance to be photodissociated. The two photon scheme is necessary because in general bound-continuum photodissociation transitions have a linewidth many orders of magnitude larger than bound-bound transitions, and so a single-photon photodissociation scheme would not be state-selective.

To ensure a sufficient photodissociation rate, the choice of second photon color must be made with consideration of the continuum states of the molecule. The calculation of photodissociation cross sections, which guides the choice of photon color, is discussed in Sec. 5.3. The dissociation is detected by mass spectrometry of the ion cloud using a

destructive technique called *q-scanning*, described in Sec. 5.4. Sec. 5.2 explains how photodissociation rate is calculated from cross section and illustrates numerically for typical experimental conditions.

5.2. Relation of cross section to photodissociation rate

Typically, REMPD is done with pulsed light sources whose power is characterized by their *fluence*, or energy per shot per area $F = I \cdot \Delta t$, where I is intensity and Δt is pulse duration. Since the applied fluence is finite, the photodissociation success rate is non unity. Estimation of the original population from an experimental measurement requires estimation of this success rate, which is a function of both fluence and photodissociation cross section and is calculated as follows.

The Poisson distribution gives the probability of a given number of events occurring in a specified time interval, assuming that these events occur at a characteristic rate and are independent of previous occurrences. Given a mean number of events per observation interval, λ, the probability of exactly k successes in an observation interval is

$$(5.1) \qquad\qquad P(k; \lambda) = \frac{\lambda^k e^{-\lambda}}{k!}.$$

This describes photoionization of a molecule since each photon independently has a probability of σ/A to cause photoionization, where σ is the cross section and A is the beam cross sectional area. Here the observation interval is chosen to be the duration of one optical pulse. Although the molecule can be photoionized only once, outcomes with two or more photoionization events during one observation interval are meaningful; they must be summed over to compute the correct probability for photoionization. Since the action of each photon is assumed independent (in that each photon has equal probability of causing photoionization, independent of previous outcomes), $\lambda = N\sigma/A$ for a pulse with N photons.

The probability of one or more photoionization events is

$$P(k \geq 1; \lambda) = \sum_{k=1}^{\infty} \frac{\lambda^k e^{-\lambda}}{k!} = e^{-\lambda} \sum_{k=1}^{\infty} \frac{\lambda^k}{k!} = e^{-\lambda}(e^{\lambda} - 1)$$

(5.2)

$$= 1 - e^{-\lambda}.$$

If this beam has intensity

(5.3)
$$I = \frac{N\hbar\omega}{\Delta t \cdot A},$$

then

(5.4)
$$\lambda = \sigma N/A = \sigma \times \frac{I\Delta t}{\hbar\omega},$$

and from Eqn. 5.2 the probability per pulse of a molecule being photoionized is

(5.5)
$$P = 1 - exp(-\frac{\sigma I \Delta t}{\hbar\omega}).$$

The full photodissociation probability is the product of Eqn. 5.5 and the probability of excitation due to the first photon. If sufficient intensity is applied driving the bound-bound transition, then the Rabi frequency will be large compared to the pulse duration, and half of the initial population will be eligible for photoionization. Eqn. 5.5 divided by two is then the full probability per pulse. The following example illustrates these ideas under typical experimental conditions.

In SiO^+, 354 nm light drives the 2-0 band and can further drive 1+1 REMPD by the $B^2\Sigma^+ \rightarrow (3)^2\Sigma^+$ channel with cross section $\sigma = 2 \cdot 10^{-19}$ cm^2 (see Sec. 5.3). At this wavelength, a Pyridine 2 dye laser, pumped at 10 Hz by 4 W of 532 nm light from

a Nd:YAG laser, produces > 5 mJ per 10 nsec pulse. The 2-0 transition has $I_{sat} = 5 \cdot 10^{-5}$ mW/cm^2 assuming a natural lifetime $\tau \approx 10$ ms. Focusing the dye output to a 200 μm beam radius causes > 10 Rabi flops per 10 nsec pulse, so it is valid to assume that half the population is eligible for photodissociation. The overall probability of photodissociation per pulse is then 37.9 %, and several pulses suffice to ensure nearly complete dissociation.

5.3. Calculation of photodissociation cross sections

The cross section for bound $\rightarrow$ continuum transitions can depend strongly on the wavelength of the driving photon. In order to ensure a choice of second photon color resulting in a reasonable REMPD rate, photodissociation cross sections have been calculated using BCONT [23], a software package for computing properties of bound $\rightarrow$ continuum transitions. This section describes the physics underlying this calculation and reviews the BCONT output.

For any single-photon transition in a diatomic molecule, the transition probability is proportional to a matrix element that can be factored into rotational, vibrational, and electronic components. The rotational contribution is called a *Hönl-London factor* and is neglected in this section as it is of order one. The vibrational contribution is the direct overlap integral between the initial and final state vibrational wavefunctions, $|<v_i|v_f>|^2$, and is called the *Franck-Condon factor*. And the electronic contribution, which involves the electronic wavefunctions and the electric dipole operator, gives the *transition dipole moment function*.

Since the vibrational wavefunctions are the eigenstates of the PECs, computing the Franck-Condon factor requires knowledge of the PECs of the bound and continuum states. Three theory groups have produced PECs for SiO^+: François [4], Das [6], and Honjou [18][17]. Das and Honjou both include state-repulsion considerations neglected by the earlier work of François, and so this section presents the BCONT results resulting from the Das and Honojou PECs.
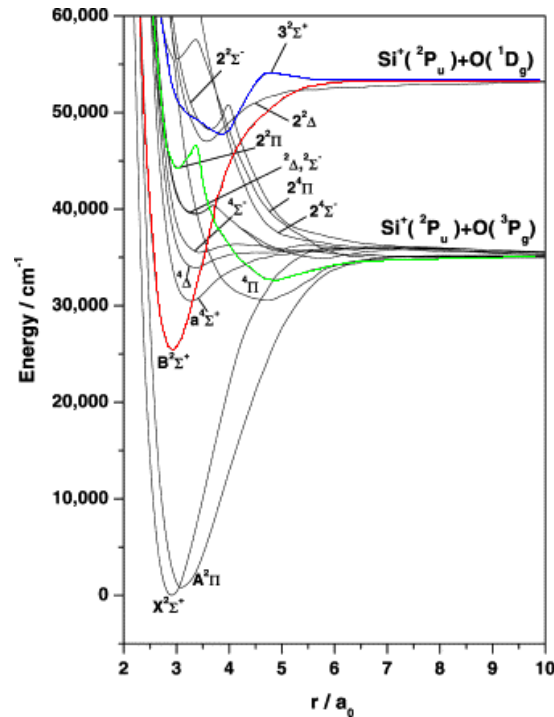
Figure 5.1. Potential energy curves for SiO^+ calculated from theory by Das [6]. Photodissociation from the B state (red) via an optical transition can proceed to any of three higher-lying states: $(2)^2\Pi$ (green), $(3)^2\Sigma^+$ (blue), or $(3)^2\Pi$ (not pictured). Figure is as produced by Das, except where color has been added to highlight relevant states. Other states lying above B are not suitable for REMPD as doublet $\rightarrow$ quadruplet transitions are forbidden, as are $\Sigma \rightarrow \Delta$ transitions.

The vertical spacing between the bound and continuum PECs sets the scale of transition energy for which the cross section is strongest. In units of wavenumber, optical transitions correspond to approximately 10,000–30,000 cm^{-1}, which can be seen in Fig. 5.1 to correspond to transitions from B to several higher-lying continuum states which have been highlighted in color. Transitions from B to other pictured states are strongly suppressed by selection rules that disallow doublet $\rightarrow$ quadruplet and $\Sigma \rightarrow \Delta$ transitions. In addition to the two usable states above B highlighted in Fig. 5.1, a third is not visible,

though is described by François and Honjou. Thus there are three available photodissociation channels: $B^2\Sigma^+ \to (2)^2\Pi$, $B^2\Sigma^+ \to (3)^2\Sigma^+$, and $B^2\Sigma^+ \to (3)^2\Pi$. Energetically, these roughly correspond to the available ND:YAG harmonics: 532 nm (second harmonic), 355 nm (third harmonic), and 266 nm (fourth harmonic), respectively, and these three colors were each used in $1+1'$ REMPD attempts.

Features of the photodissociation cross section curves resulting from these three channels can be better understood by the *Condon reflection approximation*, a method for intuiting the shape of the photodissociation curve from the PECs. For unbound PECs, the eigenfunctions are Airy functions with continuously spaced eigenvalues. The reflection approximation takes these eigenfunctions to be delta functions, which reduces the vibrational overlap integral to a reflection of bound state vibrational wavefunction (see Fig. 5.2). The result is that the plot of photodissociation cross section against transition energy mimics the shape of the bound state wavefunction; for $v'' \neq 0$, the photodissociation cross section will have v'' nodes, just as the bound wavefunction does.
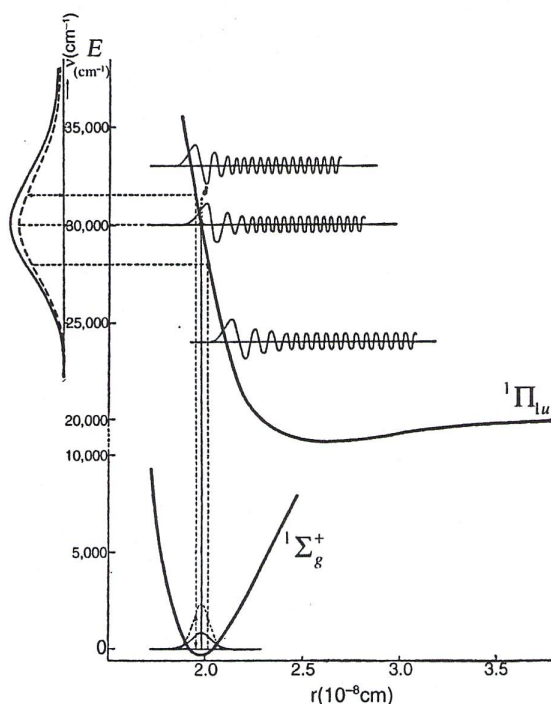
Figure 5.2. The Condon reflection approximation simplifies the computation of the vibrational overlap integral. The unbound wavefunctions are approximated as delta functions. Figure reproduced from [24].

The TDMF's for SiO^+ for these transitions are not available in the literature, either from experiment or theory. They have been estimated in unpublished work by the François group, however, and our calculation uses their values (see Table 5.1), provided to us in private communication [11].

Using the PECs from Das produces the photodissociation curves in Fig. 5.3, while using those from Honjou produces Fig. 5.4. In both cases the TDMF from François is used.

Table 5.1. Theory values of transition dipole moment functions from un-published correspondence with J.P. François. Atomic units are used, which are Bohr radii, $a_0 = 0.529$ Å, for distance and $ea_0 = 2.54$ Debye for dipole moment.

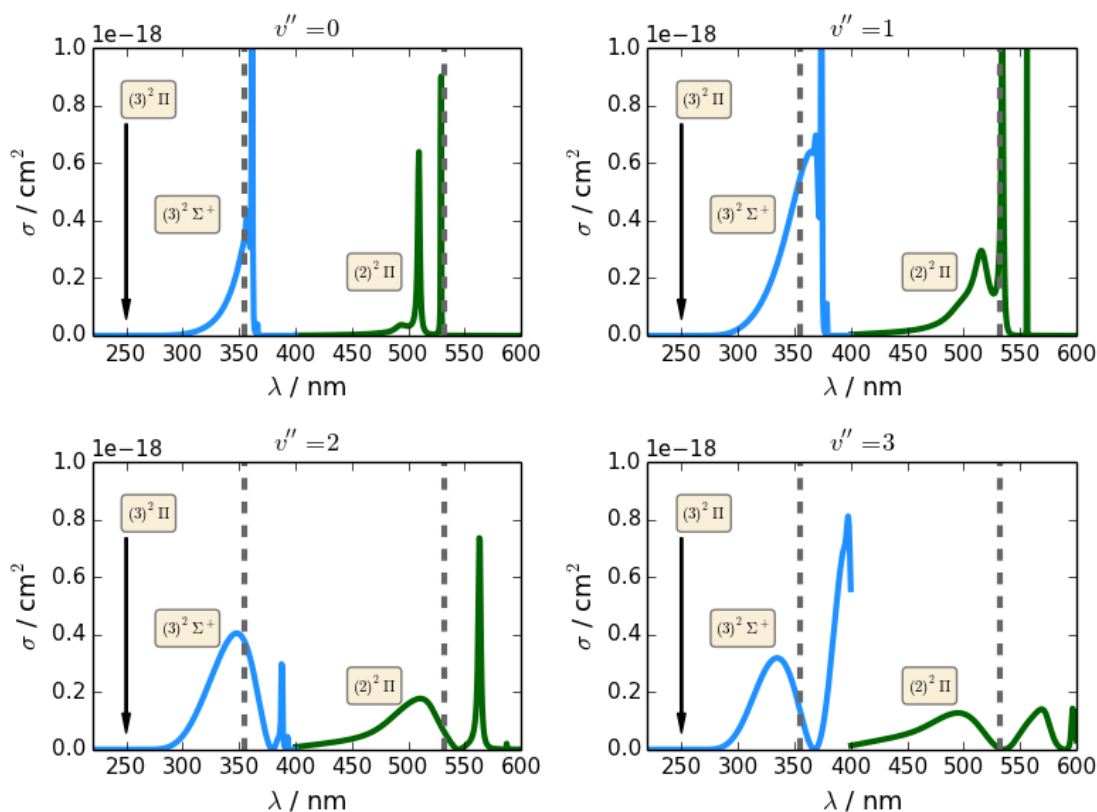|	Moment (a.u.)		
Transition	2.89	3.20	3.60
$(2)^2\Pi - B^2\Sigma^+$	0.07446	0.05019	0.02316
$(3)^2\Sigma^+ - B^2\Sigma^+$	0.17456	0.25549	0.37878
$(3)^2\Pi - B^2\Sigma^+$	0.02478	0.02921	0.08362

Figure 5.3. Photodissociation cross sections calculated using potential energy curves from Das. Dotted lines indicate easily accessible $1'$ photon wavelengths of 355 nm and 532 nm.
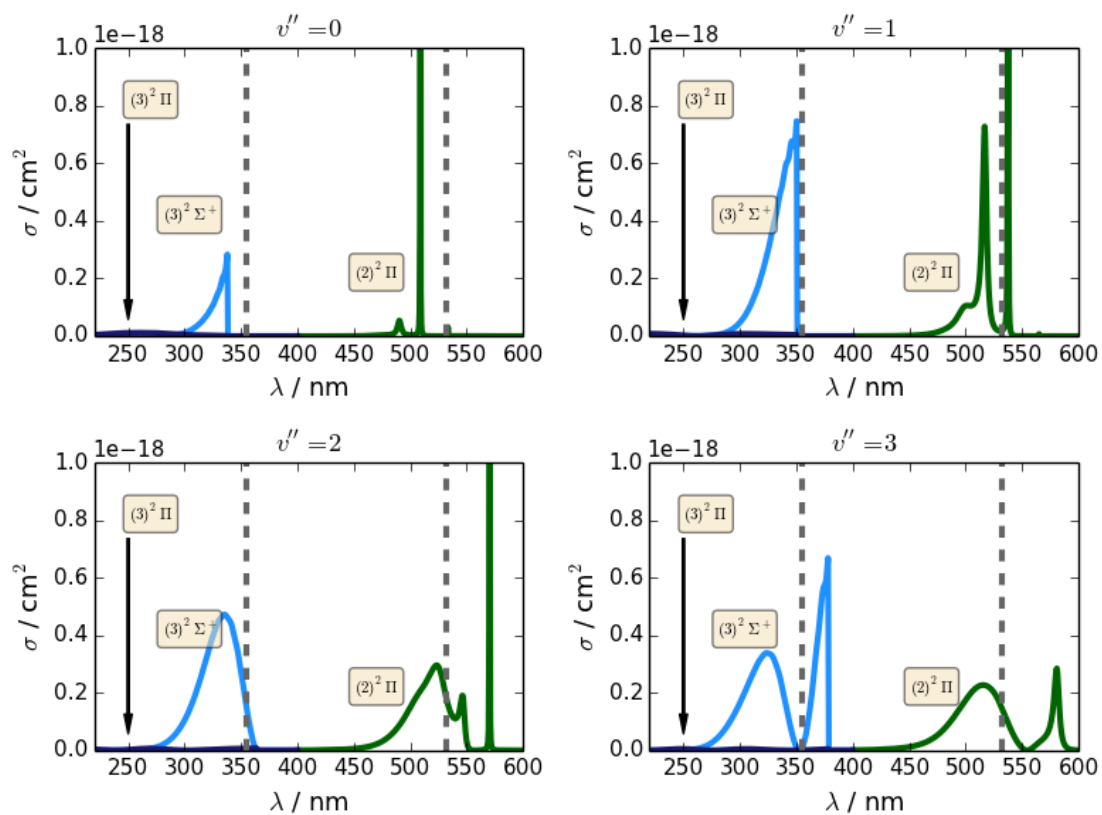
Figure 5.4. Photodissociation cross sections calculated using potential energy curves from Honjou. Dotted lines indicate easily accessible 1′ photon wavelengths of 355 nm and 532 nm.

5.4. Q-scanning

After REMPD of a target rovibrational state or states, the ratio of Si^+ to SiO^+ ions in the sample can be used to estimate the proportion of the initial population in the target state(s). *Q-scanning*, a mass-selective deloading technique, is used to generate the mass spectrum. The rf voltage amplitude is swept down to zero in the presence of a large DC bias, and because the pseudopotential confinement strength scales with mass, ions of different mass deload the trap at different rf voltage thresholds. The DC bias is due to the ion detector, a *(single-)channel electron multiplier* (CEM), positioned near the trap as shown in Fig. 5.5. The name q-scan derives from the fact that the sweeping of rf voltage amplitude can be understood in the (a,q) formalism as a sweep of the q parameter, which is proportional to rf voltage amplitude.
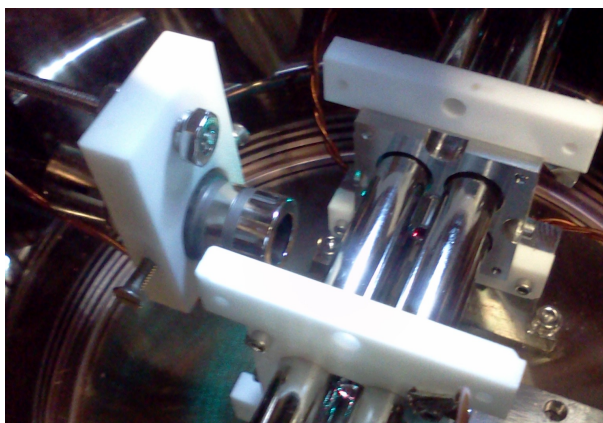
Figure 5.5. CEM positioned near trap with line-of-sight access to trapping region. When a large negative voltage is applied to the CEM, trapped ions are attracted and eventually deloaded.

The CEM operates by using a large negative voltage to attract positive ions into its collecting electrode. The impact at this electrode produces secondary electron emissions, inducing a cascade of electrons to arrive at the CEM output electrode, and following

circuitry converts this signal to a voltage. The gain of the CEM may be tuned to operate as a *digital* counter, in which a single ion saturates the output temporarily, or as an *analog* device, in which the signal amplitude is proportional to the ion count.

Although the dynamics associated with deloading a large crystal are complex, Welling provides a simple model for understanding the scaling between ion mass and the threshold rf voltage for confinement [47]. In principle, the (a,q) formalism predicts, for a=0, stability as q approaches zero. The trap depth, however, also decreases with q, so at small q the effect of perturbing fields is strong. If a uniform external electric field E_0 is applied, a lower bound on q (and hence an upper bound on mass) is induced. Equating the confining force due to the external field with the confining force due to the pseudopotential yields

$$(5.6) \qquad \frac{m}{q} = \frac{1}{2} \frac{eV_{rf}^2}{E_0 r_0^3 \Omega^2}$$

where m/q is the mass to charge ratio of the ion.

This expression permits the x-axis of each measured mass spectrum to be converted from rf voltage to mass. The rf voltage corresponding to the maximum number of ion counts is assumed to be due to Ba^+ and assigned mass 138. Other rf voltages are assigned a mass by assuming the quadratic dependence of rf voltage on m/q in Eqn. 5.6.

The quality of the mass spectrometry resulting from q-scanning is typically quantified by $m/\Delta m$, the relative width of a mass peak corresponding to a single isotopically-pure species. In the experimental setup described here, $m/\Delta m = 5\text{-}10$ is typically obtained for cooled ions, while Welling reports $m/\Delta m$ values of ≤ 5 for uncooled ions.

Experimentally, ion samples are prepared with the CEM (Burle 5900) off. The collector electrode is then adiabatically lowered to -2.8 kV (power supply used is Acopian model
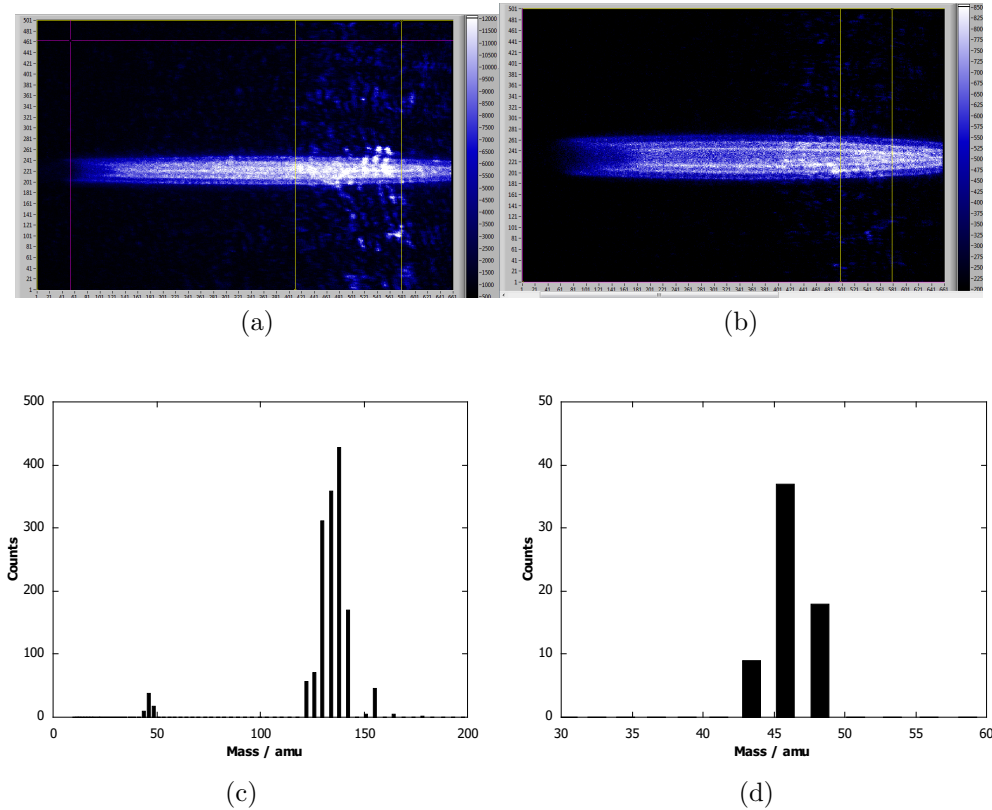
Figure 5.6. Typical mass spectrum as measured by q-scanning. (a) Ba$^+$ crystal. The dark ions at far left are isotopes of Ba$^+$ other than the 138 species used for cooling, pushed to the left side by light pressure. (b) Ba$^+$/SiO$^+$ bicrystal. The dark core visible in the center is composed of SiO$^+$. (c) Mass spectrum generated by q-scanning the bicrystal seen in (b). The mass axis is calibrated by assigning the bin with maximal counts to mass 138. (d) Expanded view of (c) focusing on the mass bins assigned to 44-SiO$^+$.

NO.35HA8.5T) while DC compensation of several tenths of a volt is applied to keep the trapped ions at their original position.

The rf voltage is generated by a function generator passed through an rf amplifier (Minicircuits TIA-1000-IR8) and into a torroidal resonator. The function generator output amplitude is controlled by an analog 0-5 volt signal which is scanned in several hundred

steps, with the CEM collecting for typically 10 μsec at each voltage step. (No additional ion counts result from collecting for longer.) Calibration of rf voltage at the trap against the 0-5 volt control voltage is performed previously by a high impedance probe attached at the resonator output, sampled in sync with the q-scan. The CEM signal is sent through an amplifier (SRS SR445A) to a digital counter (SRS SR 400) which bins the counts at each voltage step. The discriminator on the counter is set so that q-scans of an empty trap typically yield zero counts, or infrequently yield one count. Fig. 5.6 shows a typical mass spectrum.

CHAPTER 6

Reference Spectroscopy

6.1. Methodology

A spectroscopic reference locating the 0-0 band is necessary both to tune the state-selective photon in REMPD as well as position the pulse-shaping cutoff.

The method used for spectroscopy is detection of laser-induced fluorescence (LIF) from SiO^+ produced by ablation of an Si^+ sample in an O_2 environment. Spectroscopy of the B-X 0-0 band using this method was published in 1997 [26]. SiO^+ formed in the ablation plume is interrogated by a probe laser which is swept across a frequency range that contains the B-X 0-0 band. When resonant with a rotational line within this band, spontaneous emission from the resulting excited state is observed on a gated photomultiplier tube (PMT).

A schematic of the experimental apparatus is presented in Fig. 6.1. The ablation and probe pulses are both generated by Nd:YAG lasers; the direct output of one Nd:YAG laser at 1064 nm is used for ablation, while the second Nd:YAG laser pumps a dye laser.

The ablation pulse is 1064 nm and is produced by an Nd:YAG laser (Continuum Minilite II). The probe pulse is produced by pumping a dye with a second Nd:YAG laser after frequency doubling the Nd:YAG output from 1064 nm to 532 nm. The dye laser (Sirah PrecisionScan) is filled with one of several dyes that laze at 770 nm, and this output is frequency doubled to produce the 385 nm probe light.

The remainder of this section is divided into subsections addressing specific imple-
mentation issues. The methods that were observed to enhance signal strength are also
discussed. With practice, clean spectroscopy was reproducible on a daily basis with typi-
cally half an hour of set up. A list of the equipment required for this experiment is given
in Tbl. 6.1.

Timing concerns

The components of the experiment whose timing must be coordinated are: (1) the
ablation pulse, (2) the probe pulse, (3) the PMT gating. Fig. 6.2 (a) shows the desired
relative timing. The ablation pulse arrives first, producing an ablation plume that begins
to expand and move away from the sample surface. The probe pulse reaches the probe
region some time T1 later, just as the ablation products reach the probe region. The
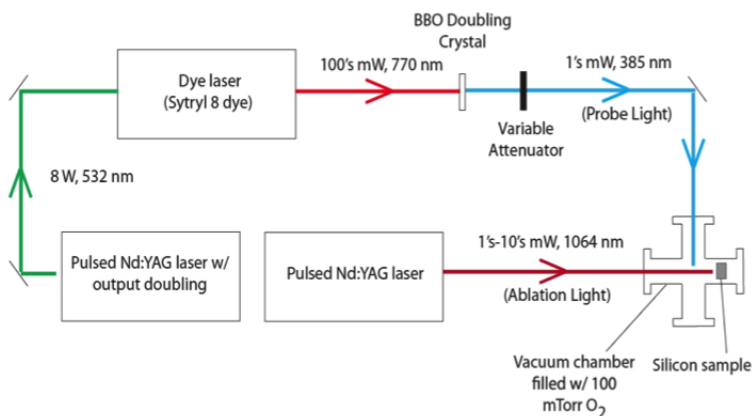PMT gate then opens at some time T2 and closes at some time T3, set to exclude the

Figure 6.1. Schematic of apparatus for SiO^+ reference spectroscopy. Laser-
induced fluorescence (LIF) is detected by a photomultiplier tube (PMT).
SiO^+ is produced by ablation of a Si sample in the presence of O_2, typically
at about 100 mTorr.

probe pulse but capture fluorescence from spontaneous decay of excited states produced by the probe.
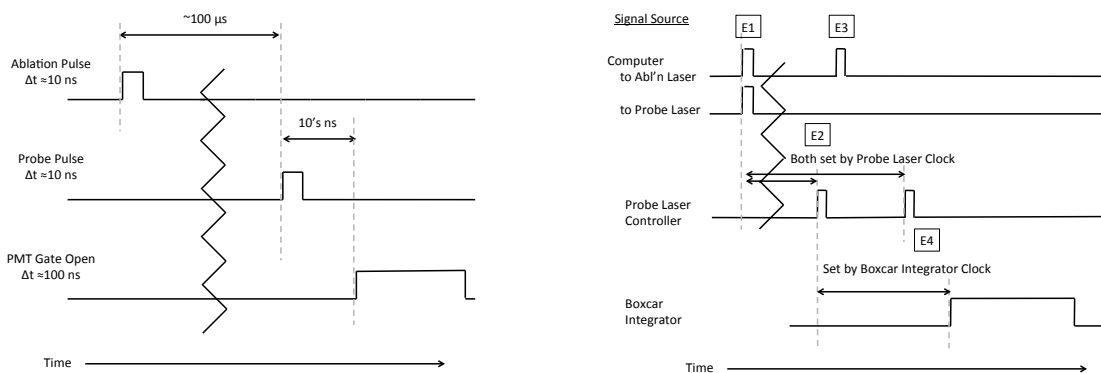
(a) Desired timing of experimental events.

(b) Timing pulses sent/received by apparatus to produce required timing.

Figure 6.2. Timing diagram for a single spectroscopic experiment, consisting of ablation, probe, and light collection. Experiments are repeated at the repetition rate of the pulse lasers, 10 Hz.

Fig. 6.2 (b) shows the timing of a Nd:YAG laser pulse is controlled by the firing first of a flashlamp (which pumps the gain medium) and then of a q-switch (which releases the circulating optical power). Mistuning of the delay between the firing of these two components reduces output power. Both Nd:YAG lasers used in this experiment allow the flashlamp to be triggered either internally or externally as well as the q-switch to be triggered internally or externally. If both are triggered internally, the laser fires pulses based on its own internal clock. If both are triggered externally, the master clock is the external trigger source.

The most demanding timing requirement in this experiment is the delay between the probe interrogation and the PMT gating. The excited state produced by driving the B-X 0-0 band has natural lifetime = 70 nsec, while the probe light scatters in the chamber for 1's to 10's of nsec after its arrival. The PMT gate must open to collect the former of these while rejecting the latter. A ones of ns relative timing repeatability is thus desired.

In the experimental realization, the maser clock for the experiment is produced from an NI-6602 timing card, which has a 80 MHz internal clock and thus has 12.5 nsec precision in relative pulse timing. For the ablation laser, both the flashlamp and ablation q-switch firing are controlled from this master clock. For the probe laser, the probe flashlamp is controlled by the master clock, but the probe q-switch is triggered by the internal clock of the probe YAG.

When its q-switch is internally triggered, the Nd:YAG produces a TTL output in advance of the q-switch firing, and this is used to trigger the PMT gating.

The gating of the PMT signal is done externally from the PMT by a boxcar integrator (SRS SR250). This gating is set on the integrator relative to a trigger, and the gating has 1's of nsec repeatability when triggered in this way.

Positioning the Si Sample

The Si sample is held in a custom fabricated mount designed by Jason Nguyen and shown in Fig. 6.3. Mechanical drawings are included in the supplemental materials to this document. When assembling the chamber, the mounting plates are adjusted until the sample is ˜10 mm from the probe beam path. Because light baffles constrain the probe beam location, setting the mounting plate locations is the only method for controlling the distance between the sample and the probe region. The probe timing is set by this

distance; ideally the probe light arrives just as the ablation plume has moved into the probe region.
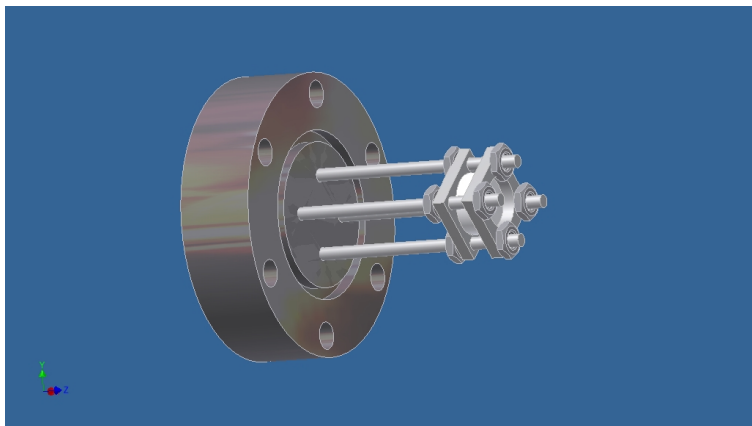
Figure 6.3. Si^+ sample holder made from modified 2.75" CF blank. Design due to Jason Nguyen. The flange surface is tapped to accept four threaded rods and custom fabricated plates mount onto the rods and clamp onto the Si^+ sample and allow mm scale tuning of the sample location.

Optimization of Ablation Behavior

A difficulty in producing a consistent signal from this experiment is that ablation produces an inconsistent sample flux. Changes in signal strength during spectroscopy runs when all experimental parameters (except probe laser frequency) were attributed to changes in sample flux. Consistently strong signal lasting more than ten minutes (at 10 Hz interrogation) was observed only rarely.

At high ablation powers (ones of mJ), the ablation plume becomes visible to the eye. The positioning of the focusing lens (the last lens before the chamber in the ablation laser beam path) was optimized by maximizing the brightness of this ablation spot, which occurred when the beam was tightly focused on the sample surface.

Effect of O_2 Pressure Tuning

To prepare the vacuum system for a spectroscopic data run, the chamber is first pumped down by rough pump and turbo pump to less than 1e-4 (the limit of the attached Convectron gauge). The Turbo pump is then turned off and allowed to slow its rotations on its own over several minutes. The valve to the turbo and rough pump is then closed. When it has sufficiently slowed to be able to pump against atmosphere, the leak valve to the O_2 inlet is opened, but only enough to observe some O_2 in the system. In practice, pressure rises to ones of Torr were typical at this stage. The valve to the Turbo was then opened slightly until a pressure drop was visible. Tightening or loosening this valve was found to be a reliable method of controlling the rate at which O_2 was pumped out of the system. When the desired pressure was reached, often 100 mTorr for first attempts to see a spectroscopy signal, the valve is closed.

Signal strength can be significantly optimized by tuning the O_2 concentration while observing the PMT signal. Carefully opening the valve to the Turbo was found to permit controlled reduction in O_2 concentration, with the PMT resonance amplitude responding directly–typically the optimized concentration was between 30 and 100 mTorr.

Minimization of Background Photon Counts

The lifetime of the excited state in the 0-0 band and the timescale for ring down of scattered probe light are of comparable timescale. An in vacuo iris, made from a 2.75" CF blank with a 1 cm diameter drilled central hole, is used as a light baffle. The probe beam is thus constrained to pass through the geometric center of the CF cross; it passes through a baffle both as it enters and as it exits.

(a) PMT signal, μsec scale, showing fluorescence from the ablation plume which may have complicated structure and persist for up to 10's of nsec.

(b) PMT signal from (a), zoomed to nsec scale during interrogation.

Figure 6.4. Example PMT signal resulting from a single experiment. (b) shows background due to the probe laser scattering in the chamber. The superimposed gate logic signal shows where the LIF signal is observed to appear.

Name	Vendor	Model Number	Comment
Boxcar Integrator	SRS	SR250	
Computer Interface Module	SRS	SR245	Supporting hardware for SR250
Power Supply	SRS	SRS280	Supporting hardware for SR250
Signal Amplifier	SRS	SR445A	4 ch, DC to 350 MHz
PMT	Hammamatsu	HRT7000	Analog PMT
1" UV Lens, f=50 mm (2)	Thorlabs	LA1131-A	PMT light collection
Translation stage (3)	Thorlabs	PT3	Collection optics positioning
Blackout material	Thorlabs	BK5	To shield collection optics
Ablation Laser	Continuum	Minilite II	
Probe Laser	Sirah	Precision Scan	
2.75" CF Viewport (4)	Duniway	VP-275-150	AR coat not essential
2.75" CF Six Way Cross	Lesker	C6-0275	
2.75" CF Nipple (2)	Duniway	NP-275	
2.75" CF Baffle (2)	PChemLabs	P104724	Custom modifications. See text.
Si sample holder	n/a	n/a	Custom modifications. See text.
1" UV Mirror (5+)	Thorlabs	E01	For 385 nm probe light
1" Nd:YAG Line Mirror (5+)	Thorlabs	NB1-K13	For ablation beam
Posts, Post Holders, Mirror Mounts	Thorlabs	Various	As needed
Lens Tubing, Mounts	Thorlabs	Various	As needed

Table 6.1. Parts list. Vacuum pumps, gauges, valves and mounting hardware may be varied and are not listed above. Mechanical stability of chamber and vacuum quality requirements are found to be modest. Vendor part numbers confirmed accurate as of February 13, 2014.

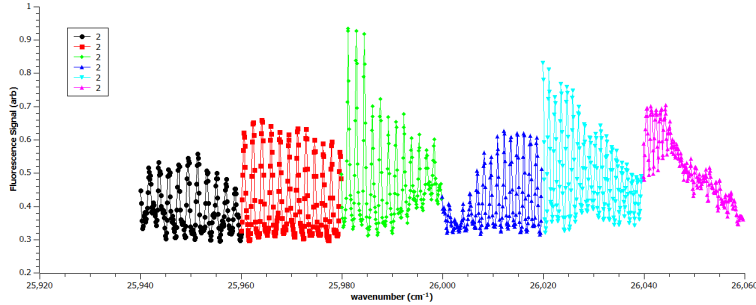## 6.2. Spectroscopic Results and Implications for Repeatability

Figure 6.5. Spectrum of the B-X 0-0 band. Full data set is composed of several sequential scans.

An example of the measured spectrum of the 0-0 band is shown in Fig. 6.5. The full data set is composed of several scans, as signal strength variability often necessitated reoptimizing experimental parameters, frequently between scans. The line width of the rotational transitions, which are dominated by Doppler broadening is observed to be ones of GHz, far greater than the natural line width of these transitions which is typically $\Gamma = 1/70$ nsec $= 14$ MHz.

The 1-0 and 2-0 bands were also investigated. The experimental signal strength of these bands was found to be weaker than the 0-0 band. These higher bands are expected to be more difficult to drive due to Franck-Condon factor suppression. The fluorescence is collected from all decay pathways, however, so the increased difficulty in observing those bands is due to insufficient saturation of the transition; indeed while μJ per shot of probe intensity was sufficient to drive the 0-0 spectroscopy, the maximum available 1's of mJ were used to recover comparable signal strength in the spectroscopy of the 1-0 and 2-0 bands.

Repeatbility issues result from the fact that the dye laser wavelength is tuned by a step motor which changes the angle of the internal grating. The accuracy to which the wavelength can be set is thus limited by the step motor repeatability. At the mK translational temperatures achieved by sympathetic cooling, the linewidths of rotational transitions in SiO^+ approach their natural linewidth $= 1/70$ nsec.

A typical data run mapping the 0-0 band, such as the one shown in Fig. 6.6 scans over a few 10's of cm^{-1}. This is a small fraction of the step motor tuning range. Since the step motor position is confirmed to map linearly over this wider tuning range, the assumption is made that it scans linearly during a given data run. Then only a calibration offset error is possible.

The positions of each rotational line is extracted from the raw data by taking the local maximum within preselected ranges. The data can then be fit to a three parameter fitting function in which the free parameters are the band head location and the rotational constants of the upper and lower state, denoted ν_0, B_e' and B_e''. The explicit functional form of the fitting curve is, for a P-branch transition from a ground state with rotational quantum number N,

$$(6.1) \qquad \nu = \nu_0 + (B_e' - B_e'')N - (B_e' + B_e'')N^2$$

and for an R-branch transition, with N as above,

$$(6.2) \qquad \nu = \nu_0 + 2B_e' - (3B_e' + B_e'')N + (B_e' - B_e'')N^2.$$

These expressions are derived from the formulae for the energies of the involved states for $^2\Sigma^+$ rotational levels given by [15].
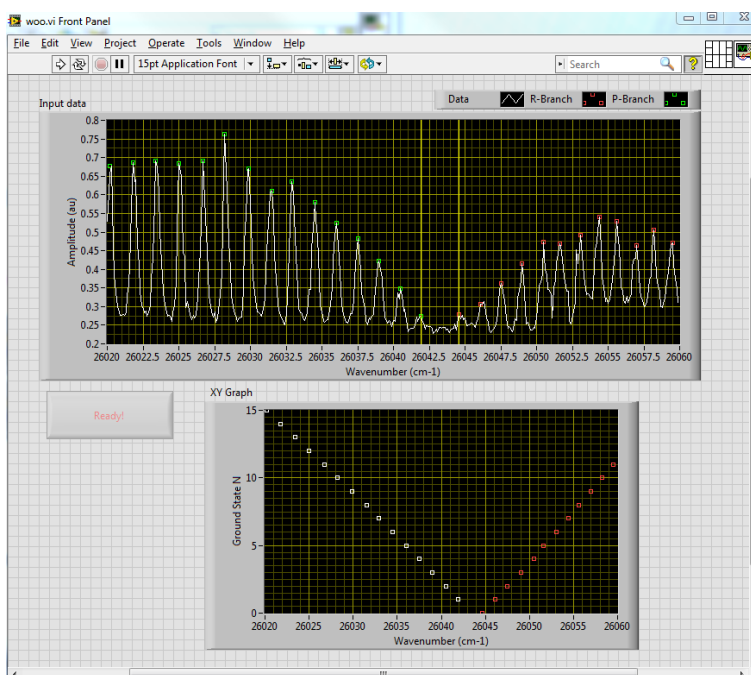
Figure 6.6. Example of fitting to rotational line locations found in a spectroscopic measurement of the 0-0 band. The fitting parameters are the band head location and the rotational constants of the upper and lower state. The fit is used to predict other rotational line locations, in particular the P1 line.

Spectroscopy of the same band is repeated several times and the fitting results compared. To facilitate comparison, the fit is used to predict the P1 location. The predicted P1 locations of successive runs are found to have small variation on the timescale of hours, but large variation from day to day. Tbl. 6.2 shows a series of predicted P1 values measured on subsequent days. The predicted values from a given day are seen to cluster together with small variation compared to the day-to-day shift. This shift is also large compared to the natural linewidth of the rotational transitions, indicating that each day the dye laser must be calibrated to be repeatable to the order of rotational line widths.

Sensors measuring temperature and relative humidity were installed and some correlation between P1 drift and lab conditions was apparent. Predicting the P1 shift from lab conditions proved imprecise, however, so daily recalibration of the probe sweep was performed. The sensor data are available in the lab notebooks.

Date	Time	Band	Predicted P1 location (cm^{-1})
Feb 8, 2013	11:25	0-0	26043.44
Feb 8, 2013	14:20	0-0	26043.26
Feb 18, 2013	17:00	0-0	26042.91
Feb 20, 2013	9:45	0-0	26043.31
Feb 20, 2013	9:50	0-0	26043.33
Feb 20, 2013	9:55	0-0	26043.32
Feb 20, 2013	10:00	0-0	26043.35

Table 6.2. Selected results of repeated SiO^+ spectroscopy illustrating day-to-day drift of absolute probe calibration. The location of the P1 transition is predicted from each scan, and the variability in this value demonstrates the need for daily frequency recalibration.

References

[1] Milton Abramowitz and Irene A. Stegun, *Handbook of mathematical functions with formulas, graphs, and mathematical tables*, ninth dover printing, tenth gpo printing ed., Dover, New York, 1964.

[2] R. Alheit, S. Kleineidam, F. Vedel, M. Vedel, and G. Werth, *Higher order nonlinear resonances in a paul trap*, International Journal of Mass Spectrometry and Ion Processes **154** (1996), no. 3, 155 – 169.

[3] P. Blythe, B. Roth, U. Fröhlich, H. Wenz, and S. Schiller, *Production of ultracold trapped molecular hydrogen ions*, Phys. Rev. Lett. **95** (2005), no. 18, 183002.

[4] Z. Cai and J.P. François, *Ab initio study of the electronic spectrum of the sio(+) cation.*, J Mol Spectrosc **197** (1999), no. 1, 12–18.

[5] R Cameron, TJ Scholl, L Zhang, RA Holt, and SD Rosner, *Fast-ion-beam laser spectroscopy of the b2σ+-x2σ+ and b2σ+-a2π systems of sio+: Deperturbation analysis*, Journal of Molecular Spectroscopy **169** (1995), no. 2, 364–372.

[6] Surya Chattopadhyaya, Anjan Chattopadhyay, and Kalyan Kumar Das, *Electronic spectrum of sio¡ sup¿+¡/sup¿: a theoretical study*, Journal of Molecular Structure (Thermochem) **639** (2003), no. 1, 177–185.

[7] H. G. Dehmelt, *Radiofrequency spectroscopy of stored ions*, Adv. At. Mol. Opt. Phys. **3** (1967), 53–72.

[8] A. Drakoudis, M. Söllner, and G. Werth, *Instabilities of ion motion in a linear paul trap*, International Journal of Mass Spectrometry **252** (2006), no. 1, 61 – 68.

[9] M. Drewsen, C. Brodersen, L. Hornekær, J. S. Hangst, and J. P. Schiffer, *Large ion crystals in a linear paul trap*, Physical Review Letters **81** (1998), no. 14, 2878.

[10] Daniel H. E. Dubin and T. M. O'Neil, *Trapped nonneutral plasmas, liquids, and crystals (the thermal equilibrium states)*, Reviews of Modern Physics **71** (1999), no. 1, 87–172.

[11] J.P. François, *Dipole-allowed transition moments*, private communication, 2013.

[12] Christophe Geuzaine and Jean-Franois Remacle, *Gmsh: A 3-d finite element mesh generator with built-in pre- and post-processing facilities*, International Journal for Numerical Methods in Engineering **79** (2009), no. 11, 1309–1331.

[13] H. Haffner, W. Hansel, C. F. Roos, J. Benhelm, D. Chek al kar, M. Chwalla, T. Korber, U. D. Rapol, M. Riebe, P. O. Schmidt, C. Becher, O. Guhne, W. Dur, and R. Blatt, *Scalable multiparticle entanglement of trapped ions*, Nature **438** (2005), no. 7068, 643–646.

[14] Peter F. Herskind, Aurelien Dantan, Joan P. Marler, Magnus Albert, and Michael Drewsen, *Realization of collective strong coupling with ion coulomb crystals in an optical cavity*, Nat Phys **5** (2009), no. 7, 494–498.

[15] G. Herzberg, *Molecular spectra and molecular structure - vol. i*, Molecular Spectra and Molecular Structure, Read Books, 2007.

[16] Robert C Hilborn, *Einstein coefficients, cross sections, f values, dipole moments, and all that*, American Journal of Physics **50** (1982), 982.

[17] Nobumitsu Honjou, *Ab initio configuration interaction study on the electronic structure of the 1–42π states of sio+ and the avoided crossings of the 2–42π potential energy curves*, Molecular Physics **101** (2003), no. 20, 3063–3071.

[18] ———, *Ab initio configuration interaction study on the electronic structure of the x2σ+, b2σ+ and 32σ+ states of sio+*, Molecular Physics **101** (2003), no. 1-2, 131–141.

[19] D B Hume, T Rosenband, and D J Wineland, *High-fidelity adaptive qubit detection through repetitive quantum nondemolition measurements*, Physical Review Letters **99** (2007), no. 12, 120502.

[20] Setsuo Ichimaru, *Strongly coupled plasmas: high-density classical plasmas and degenerate electron liquids*, Rev. Mod. Phys. **54** (1982), no. 4, 1017–1059.

[21] J. C. J. Koelemeij, B. Roth, A. Wicht, I. Ernsting, and S. Schiller, *Vibrational spectroscopy of hd$^+$ with 2-ppb accuracy*, Phys. Rev. Lett. **98** (2007), no. 17, 173002.

[22] RJ Le Roy, *Level 8.0: A computer program for solving the radial schrödinger equation for bound and quasibound levels*, University of Waterloo Chemical Physics Research Report CP-663 (2007).

[23] RJ Le Roy and GT Kraemer, *Bcont 2.0. computer program for calculating absorption coefficients, emission intensities or (golden rule) predissociation rates*, University of Waterloo Chemical Physics Research Rep. CP-650 (University of Waterloo, Waterloo, Ontario, Canada, 2001). The source code and manual for this program may be obtained from the internet site http://leroy. uwaterloo. ca (2004).

[24] H. Lefebvre-Brion and R.W. Field, *The spectra and dynamics of diatomic molecules*, Elsevier Academic Press, 2004.

[25] Chien-Yu Lien, Scott R Williams, and Brian Odom, *Optical pulse-shaping for internal cooling of molecules*, Physical Chemistry Chemical Physics **13** (2011), no. 42, 18825–18829.

[26] Yukari Matsuo, Takashi Nakajima, Tohru Kobayashi, and Michio Takami, *Formation and laser-induced-fluorescence study of sio¡ equation¿¡ sup¿+¡/sup¿¡/equation¿ ions produced by laser ablation of si in oxygen gas*, Applied physics letters **71** (1997), no. 8, 996–998.

[27] N. W McLachlan, *Theory and application of mathieu functions*, first edition ed., Clarendon Press, 1947.

[28] K. Mølhave and M. Drewsen, *Formation of translationally cold mgh^+ and mgd^+ molecules in an ion trap*, Phys. Rev. A **62** (2000), no. 1, 011401.

[29] Wolfgang Paul, *Electromagnetic traps for charged and neutral particles*, Rev. Mod. Phys. **62** (1990), no. 3, 531–540.

[30] J. Pedregosa, C. Champenois, M. Houssin, and M. Knoop, *Anharmonic contributions in real rf linear quadrupole traps*, International Journal of Mass Spectrometry **290** (2010), no. 2-3, 100 – 105.

[31] J. D. Prestage, G. J. Dick, and L. Maleki, *New ion trap for frequency standard applications*, Journal of Applied Physics **66** (1989), no. 3, 1013–1017.

[32] S Removille, R Dubessy, B Dubost, Q Glorieux, T Coudreau, S Guibal, J-P Likforman, and L Guidoni, *Trapping and cooling of sr + ions: strings and large clouds*, Journal of Physics B: Atomic, Molecular and Optical Physics **42** (2009), no. 15, 154014.

[33] A. J. Reuben, G. B. Smith, P. Moses, A. V. Vagov, M. D. Woods, D. B. Gordon, and R. W. Munn, *Ion trajectories in exactly determined quadrupole fields*, International Journal of Mass Spectrometry and Ion Processes **154** (1996), no. 1-2, 43–59.

[34] T. Rosenband, D. B. Hume, P. O. Schmidt, C. W. Chou, A. Brusch, L. Lorini, W. H. Oskay, R. E. Drullinger, T. M. Fortier, J. E. Stalnaker, S. A. Diddams, W. C. Swann, N. R. Newbury, W. M. Itano, D. J. Wineland, and J. C. Bergquist, *Frequency Ratio of Al+ and Hg+ Single-Ion Optical Clocks; Metrology at the 17th Decimal Place*, Science **319** (2008), no. 5871, 1808–1812.

[35] SD Rosner, R Cameron, TJ Scholl, and RA Holt, *A study of the¡ i¿ x¡/i¿¡ sup¿ 2¡/sup¿ σ¡ sup¿+¡/sup¿ and¡ i¿ a¡/i¿¡ sup¿ 2¡/sup¿ π states of sio¡ sup¿+¡/sup¿ using fast-ion-beam laser spectroscopy*, Journal of molecular spectroscopy **189** (1998), no. 1, 83–94.

[36] Vladimir L. Ryjkov, X.Z. Zhao, and Hans A. Schuessler, *Simulations of the rf heating rates in a linear quadrupole ion trap*, Physical Review A **71** (2005), no. 3, 033414.

[37] J. P. Schiffer, M. Drewsen, J. S. Hangst, and L. Hornekær, *Temperature, ordering, and equilibrium with time-dependent confining forces*, Proceedings of the National Academy of Sciences of the United States of America **97** (2000), no. 20, 10697–10700.

[38] Tobias Schneider, B Roth, H Duncker, I Ernsting, and S Schiller, *All-optical preparation of molecular ions in the rovibrational ground state*, Nature Physics **6** (2010), no. 4, 275–278.

[39] Dimitris Sofikitis, Ridha Horchani, Xiaolin Li, Marin Pichler, Maria Allegrini, Andrea Fioretti, Daniel Comparat, and Pierre Pillet, *Vibrational cooling of cesium molecules using noncoherent broadband light*, Physical Review A **80** (2009), no. 5, 051401.

[40] Dimitris Sofikitis, Sebastien Weber, Andrea Fioretti, Ridha Horchani, Maria Allegrini, Béatrice Chatel, Daniel Comparat, and Pierre Pillet, *Molecular vibrational cooling by optical pumping with shaped femtosecond pulses*, New Journal of Physics **11** (2009), no. 5, 055037.

[41] Peter F Staanum, Klaus Højbjerre, Peter S Skyt, Anders K Hansen, and Michael Drewsen, *Rotational laser cooling of vibrationally and translationally cold molecular ions*, Nature Physics **6** (2010), no. 4, 271–274.

[42] D. A. Tabor, V Rajagopal, Y-W Lin, and B Odom, *Suitability of linear quadrupole ion traps for large coulomb crystals*, Applied Physics B **107** (2012), no. 4, 1097–1104.

[43] Matthieu Viteau, Amodsen Chotia, Maria Allegrini, Nadia Bouloufa, Olivier Dulieu, Daniel Comparat, and Pierre Pillet, *Optical pumping and vibrational cooling of molecules*, Science **321** (2008), no. 5886, 232–234.

[44] Y. Wang, J. Franzen, and K. P. Wanczek, *The non-linear resonance ion trap. part 2. a general theoretical analysis*, International Journal of Mass Spectrometry and Ion Processes **124** (1993), no. 2, 125–144.

[45] James KG Watson, *Hönl–london factors for multiplet transitions in hunds case¡ i¿ a¡/i¿ or¡ i¿ b¡/i¿*, Journal of Molecular Spectroscopy **252** (2008), no. 1, 5–8.

[46] AM Weiner, *Femtosecond pulse shaping using spatial light modulators*, Review of scientific instruments **71** (2000), no. 5, 1929–1960.

[47] M. Welling, H.A. Schuessler, R.I. Thompson, and H. Walther, *Ion/molecule reactions, mass spectrometry and optical spectroscopy in a linear ion trap*, International Journal of Mass Spectrometry and Ion Processes **172** (1998), no. 12, 95 – 114.

[48] Hans-Joachim Werner, Pavel Rosmus, and Michael Grimm, *Ab initio calculations of radiative transition probabilities in the x¡ sup¿ 1¡/sup¿ σ¡ sup¿+¡/sup¿ state of sio and the x¡ sup¿ 2¡/sup¿ σ¡ sup¿+¡/sup¿ and a¡ sup¿ 2¡/sup¿ π states of sio¡ sup¿+¡/sup¿*, Chemical Physics **73** (1982), no. 1, 169–178.

[49] Stefan Willitsch, Martin T Bell, Alexander D Gingell, and Timothy P Softley, *Chemical applications of laser- and sympathetically-cooled ions in ion traps*, Phys. Chem. Chem. Phys. **10** (2008), 7200–7210.

[50] D.J. Wineland, C. Monroe, W. M. Itano, D. Leibfried, B. E. King, and D. M. Meekhof, *Experimental issues in coherent quantum-state manipulation of trapped atomic ions*, 1998.